

# Interpreting uncertainty in Bayesian cluster analysis

Cecilia Balocchi and Sara Wade

## Abstract

The Bayesian approach to clustering is often appreciated for its ability to provide uncertainty in the partition structure. However, summarizing the posterior distribution over the clustering structure can be challenging, due to the discrete, unordered nature and massive dimension of the space. While recent advancements provide a single clustering estimate to represent the posterior, this ignores uncertainty and may even be unrepresentative in instances where the posterior is multimodal. To enhance our understanding of uncertainty, we propose a Wasserstein Approximation for Bayesian clusterIng (WASABI), which summarizes the posterior samples with not one, but multiple clustering estimates, each corresponding to a different part of the partition space that receives substantial posterior mass. Specifically, we find such clustering estimates by approximating the posterior distribution in a Wasserstein distance sense, equipped with a suitable metric on the partition space. An interesting byproduct is that a locally optimal solution can be found using a k-medoids-like algorithm on the partition space to divide the posterior samples into groups, each represented by one of the clustering estimates. Using synthetic and real datasets, we show that WASABI helps to improve the understanding of uncertainty, particularly when clusters are not well separated or when the employed model is misspecified.

## 1 Introduction

Clustering is one of the canonical forms of unsupervised learning and has numerous applications in various contexts, from finance and economics [Saunders, 1980], to natural language processing and computer science [Blei et al., 2003], biomedicine [Oyelade et al., 2016] and more. It aims to discover groups of similar data points and characterize the patterns within. While algorithmic schemes, such as k-means [Hartigan and Wong, 1979], are widely used, only a single clustering solution is provided, without any measure of uncertainty in the solution. To overcome this, the Bayesian approach is a natural choice. Through Bayes rule, the prior over the space of clusterings is combined with the model (or loss) to assess homogeneity within group, producing posterior beliefs and uncertainty for all possible clustering structures and patterns within each cluster.

However, interpreting this posterior over the clustering structure can be daunting, due to the huge dimension and discrete, unordered nature of the space of partitions. Indeed, the number of clusters is rarely known in practice, and many Bayesian methods account for this uncertainty, further increasing the dimension of the space. For example, in a Bayesian nonparametric (BNP) setting, allowing anywhere between 1 and  $n$  clusters, the total number of ways to partition the data is a Bell number, which is  $B_{20} = 51,724,158,235,372$  for only 20 data points. Even if the number of clusters is restricted in a parametric setting, the number of possible partitions is still massive, e.g. restricting to at most 5 clusters, there are still 795,019,337,135 possible clusterings of 20 data points.

Clearly, this makes any exact posterior computations infeasible, and to overcome this, Markov chain Monte Carlo (MCMC) is the most common tool. MCMC provides tens of thousands of clustering solutions, representing (asymptotically exact) draws from the posterior. Due to high dimension of the space, almost all of these clustering solutions are unique and describing the behavior and uncertainty across them is far from straightforward. Alternative inference procedures can also be used, such as importance sampling [Zhang and Williamson, 2019], sequential Monte Carlo [MacEachern et al., 1999], or posterior bootstrap [Fong et al., 2019], which similarly provide a very large number of different clustering solutions. An increasingly used alternative to posterior simulation is approximate optimization-based techniques, such as variational inference (VI). However, VI is known to suffer from mode collapse, with the approximate posterior concentrating around a single clustering solution and

providing unrealistic measures of certainty. An approach to overcome this combines multiple variational approximations through ensembles or stacking [Yao et al., 2022], which similarly produces a large number of different clustering solutions. Ensembles are also used to combat poor mixing of MCMC in high-dimensions through consensus clustering [Coleman et al., 2022].

When faced with the challenge of describing the numerous clustering solutions produced by these inference algorithms, a first task is to find a single representative clustering. From a decision-theoretic view, the optimal Bayes estimator of the clustering is found by minimizing the posterior expected loss. This requires the choice of an appropriate loss on the space of partitions, and the 0-1 loss is a simple choice, resulting in the maximum a posteriori (MAP) partition estimator. However, the 0-1 loss between two partitions is zero if and only if they coincide, and it equally penalizes any two different partitions, irrespective of how similar or different they are. This property makes the 0-1 loss unappealing. Thus, more general losses are required and have been used, such as Binder’s loss [Binder, 1978, Dahl, 2006, Lau and Green, 2007], the adjusted Rand Index [ARI, Fritsch and Ickstadt, 2009], the variation of information [VI, Meilă, 2007, Wade and Ghahramani, 2018], the normalized VI [Vinh et al., 2010, Rastelli and Friel, 2018], the generalized Binder’s loss and VI [Dahl et al., 2022], among others [Quintana and Iglesias, 2003, Franzolini and Rebaudo, 2024, Buch et al., 2024, Nguyen and Müller, 2024]. However, these methods focus on a single optimal clustering estimate (a critical aspect also highlighted in the discussion of Rastelli and Friel [2018], Dahl et al. [2022]).

Beyond providing a single clustering solution, a main motivation for the Bayesian approach is the additional uncertainty in the clustering structure. Thus, tools are also required to visualize and describe this uncertainty, which again is difficult due to the sheer number of partitions, combined with the variable number of clusters and label-switching. One important tool is the posterior similarity matrix (PSM), whose elements represent the posterior probability that a pair of data points are clustered together (also referred to as the co-clustering or consensus matrix). Additionally, Wade and Ghahramani [2018] developed credible balls to characterize uncertainty around the clustering estimate, but accurate estimation of the bounds of the credible ball based on the MCMC draws can be challenging in certain cases due to massive dimension of the partition space. An alternative greedy approach to compute the credible bounds, that allows searching beyond the MCMC draws, is presented in Buch et al. [2024]. Another approach [Lavigne and Liverani, 2024] approximates and visualizes uncertainty in the allocation of each data point, but only provides a limited view of uncertainty by conditioning on the allocation of all other points. Lastly, Do et al. [2024] represent uncertainty in the underlying mixing measure for Gaussian mixtures through a dendrogram.

In this work, we contribute an important novel tool to enhance our understanding of uncertainty in the posterior on partitions, that is applicable to the wide range of Bayesian clustering models for diverse data types. As an illustrative toy example, consider data generated from a slightly bimodal mixture of Gaussians (Figure 1a). A common paradox in BNP mixture models, such as the popular Dirichlet process mixture [DPM, Lo, 1984], is that the marginal posterior on the number of clusters may suffer from inconsistency and overestimation [Miller and Harrison, 2014, Ohn and Lin, 2023, Ascolani et al., 2023, Alamichel et al., 2024], if hyperparameters are not appropriately tuned; yet, the optimal clustering estimate can still recover the true structure under appropriate choice of loss (see Rajkowski [2019] for a theoretical analysis of the MAP and Wade [2023] for an empirical analysis of the MAP, VI, and Binder). However, when the clusters are not well separated, Rajkowski [2019] shows that the MAP underestimates the number of clusters. Indeed, in the slightly bimodal example, the MAP and VI estimate only contain a single cluster, while the ARI and Binder overestimate with 4 and 59 clusters, respectively (see Section D.1 of the Appendix). The posterior similarity matrix (Figure 1c) suggests possible additional clusters and further examination of the posterior on partitions (Figure 1b) shows multimodality. Starting from the MAP partition with a single cluster, the posterior mass decreases slightly when a single data point is split off, and continues to decrease as we increase the size of the small cluster and move further from the MAP. But, it starts to increase for more distant partitions with two clusters of more equal size.

To capture this multimodality and describe the main clustering patterns present across the posterior, we propose to summarize the posterior with not one, but multiple optimal partitions, found by minimizing the Wasserstein distance equipped with an appropriate loss. Our WASSerstein Approx-

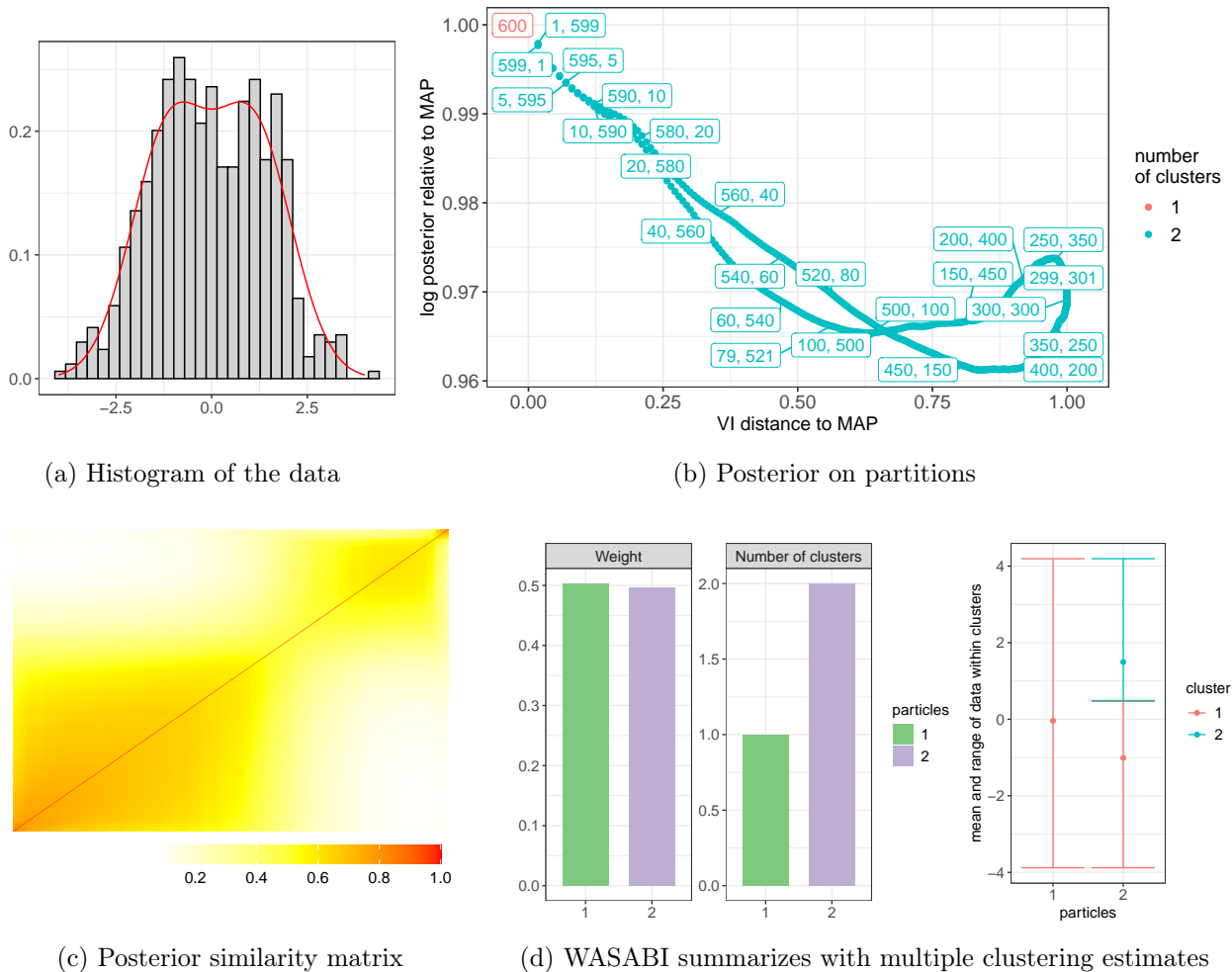


Figure 1: Slightly bimodal example. The MAP partition of a DPM for data generated from a slightly bimodal mixture (Figure 1a) contains only a single cluster, yet the posterior similarity matrix (Figure 1c) suggests uncertainty in additional clusters. To further examine the posterior on the space of partitions, Figure 1b shows the log posterior relative to the MAP against the VI distance to the MAP, where each point represents a partition colored by its number of clusters, with cluster sizes reported for some (the set of partitions plotted consists of the MAP and those with 2 clusters that respect the order of the observed data). Multimodality in the posterior is evident with one mode corresponding to the MAP and another around partitions with two clusters of more equal size. WASABI summarizes with multiple, weighted partitions (Figure 1d), reflecting the two different modes of clustering in this example.

imation for Bayesian clusterIng (WASABI) also provides weights attached to the optimal partitions (referred to as particles) and reflects the different modes of clustering in the slightly bimodal example (Figure 1d). We focus on the VI loss, due to its benefits shown in Wade and Ghahramani [2018], Rastelli and Friel [2018], Dahl et al. [2022], but other losses can be considered. This builds on the idea of Balocchi et al. [2023], who proposed an ensemble optimization method that approximates the posterior by targeting several partition estimates through minimization of the Kullback-Leibler divergence. Instead, we use the Wasserstein distance, motivated by its role in hierarchical modeling and clustering. Indeed, it has been shown to be the natural distance metric for convergence theory of mixing measures [Nguyen, 2013, Ho and Nguyen, 2016, Guha et al., 2021]. Furthermore, the Wasserstein distance is one of the few distances that allows measuring the discrepancy between distributions based on an arbitrary metric on the space on which they are supported. An interesting byproduct of using the Wasserstein distance is that the problem of determining the optimal discrete distribution with minimal Wasserstein distance from the empirical distribution can be directly linked to k-medoids clustering [Pollard, 1982, Canas and Rosasco, 2012]. As a consequence, the tool we propose can be seen as employing

k-medoids clustering to divide the samples into distinct groups and using the medoids as optimal partitions summarizing the multiple modes of the posterior. This will greatly enhance researchers’ toolbox to better describe and communicate findings and showcase the benefits of the uncertainty provided by the Bayesian approach to clustering. The code implementing the WASABI algorithm is available as an R package at <https://github.com/cecilia-balocchi/WASABI>.

## 2 Review

In the context of clustering, the observed data consists of measurements  $\mathbf{y} = (y_1, \dots, y_n)$  drawn from a heterogeneous population consisting of an unknown number homogeneous sub-populations. The observed  $y_i \in \mathcal{Y}$  may be continuous, discrete, mixed, or more complex in nature (e.g. functional data). Each data point is associated with a discrete latent variable  $c_i$  (also called the allocation variable) indicating the group membership of the data point, i.e.  $c_i = j$  if  $y_i$  belongs to the  $j$ th group, and  $c_i = c_{i'}$  if  $y_i$  and  $y_{i'}$  belong to the same sub-population. We are interested in obtaining estimates and understanding the uncertainty of clustering structure characterized by the latent  $\rho_n = (c_1, \dots, c_n)$ . To achieve this, the Bayesian approach constructs the posterior distribution

$$\pi(\rho_n | \mathbf{y}) \propto p(\mathbf{y} | \rho_n) \pi(\rho_n), \quad (1)$$

where  $\pi(\rho_n)$  represents the prior over the space of partitions and  $p(\mathbf{y} | \rho_n)$  is the likelihood in a model-based approach or defined based on a loss function in a generalized Bayes approach [Rigon et al., 2023]. For reviews of Bayesian clustering, we refer the reader to Wade [2023], Grazian [2023].

It is worth emphasizing that clustering is often referred to as an ill-posed problem, as it aims to discover unknown patterns or structures in the data. The notion of a cluster depends on the application at hand and can be challenging to characterize formally. There is often no unique clustering solution [Hennig, 2015]. Thus, one must carefully consider the model or loss employed and importantly, also characterize uncertainty in the clustering solution. To achieve the latter, Bayesian cluster analysis provides a formal framework through the posterior distribution over the entire space of clusterings. Moreover, this helps to mitigate sensitivity to local optima which adversely impacts all clustering algorithms due to the sheer size of the space.

### 2.1 Random Partition Models

A key ingredient in the Bayesian approach is the prior  $\pi(\rho_n)$  on the partition space. This is referred to as *random partition model*, as it involves randomly assigning observations to clusters, or equivalently, randomly partitioning the indices of the data points  $\{1, \dots, n\}$  into  $K_n$  non-empty and mutually exhaustive sets  $C_j$  for  $j = 1, \dots, K_n$ , where  $K_n$  represents the number of clusters. Thus, the partition  $\rho_n$  can also be represented as  $\rho_n = \{C_1, \dots, C_{K_n}\}$ , where the sets satisfy  $C_j \cap C_{j'} = \emptyset$  for  $j \neq j'$  and  $C_1 \cup \dots \cup C_{K_n} = \{1, \dots, n\}$ ; essentially, each  $C_j$  contains the indices of data points in the  $j$ th cluster. For ease of notation, the sample size is dropped from  $\rho_n$  and  $K_n$ , when the context is clear.

In practice, the number of clusters  $K$  is rarely known, and choosing this number is an important concern in cluster analysis. While information criteria or model selection tools, such as the Bayesian information criterion (BIC), are commonly used, this ignores uncertainty in the number of clusters and disregards information from the numerous models fits using different choices of  $K$ . Instead, our focus is approaches that account for this uncertainty, namely, through 1) mixtures of finite mixtures, which naturally incorporate a prior on the unknown  $K$  [Miller and Harrison, 2018, Nobile and Fearnside, 2007, Richardson and Green, 1997]; 2) sparse overfitted mixtures that specify an upper bound on the number of clusters and empty extra components through sparsity promoting priors [Rousseau and Mengersen, 2011, Malsiner-Walli et al., 2016, Frühwirth-Schnatter et al., 2021]; and 3) Bayesian nonparametric (BNP) mixtures [Müller, 2019] that allow the number of clusters to grow unboundedly with the data. For example, letting  $L$  denote an upper bound on  $K$  and  $\gamma > 0$ , the random partition model for the overfitted mixture (with a Dirichlet prior on the mixture weights) is

$$\pi(\rho) = \frac{\Gamma(\gamma L) L!}{\Gamma(\gamma L + n) (L - K)!} \prod_{j=1}^K \frac{\Gamma(n_j + \gamma)}{\Gamma(\gamma)},$$

with  $n_j = |C_j|$  denoting the cluster size. In general, random partition models specify priors on the discrete, partially-ordered space of partitions, denoted by  $\mathcal{P}$ , which has massive dimension, even more so when accounting for the unknown number of clusters.

## 2.2 Inference

The massive dimension makes computing the posterior in eq. (1) infeasible. Instead, MCMC is commonly used to obtain asymptotically exact draws, denoted by  $\rho^{(t)}$  for  $t = 1, \dots, T$ . The number of draws is typically in the tens to hundreds of thousands, and the  $\rho^{(t)}$  are mostly unique (due to the size of the space), vary in the number of clusters, and suffer from label-switching.

To provide a single, representative clustering solution, the optimal Bayes estimator minimizes the posterior expected loss. For a partition-specific loss, Wade and Ghahramani [2018] recommend the Variation of Information (VI) [Meilă, 2007], which for any two partitions  $\rho_1$  and  $\rho_2$  is defined as:

$$d_{\text{VI}}(\rho_1, \rho_2) = H(\rho_1) + H(\rho_2) - 2\text{MI}(\rho_1, \rho_2) \\ = - \sum_{j_1=1}^{K_1} \frac{n_{j_1,+}}{n} \log_2 \left( \frac{n_{j_1,+}}{n} \right) - \sum_{j_2=1}^{K_2} \frac{n_{+,j_2}}{n} \log_2 \left( \frac{n_{+,j_2}}{n} \right) - 2 \sum_{j_1=1}^{K_1} \sum_{j_2=1}^{K_2} \frac{n_{j_1,j_2}}{n} \log_2 \left( \frac{n_{j_1,j_2} n}{n_{j_1,+} n_{+,j_2}} \right),$$

where the first two terms represent the entropy of the two partitions and the last term is the mutual information between the partitions. The counts  $n_{j_1,j_2}$  represent the cross-tabulation between the partitions, i.e.  $n_{j_1,j_2}$  is the number of data points in cluster  $j_1$  in  $\rho_1$  and cluster  $j_2$  in  $\rho_2$ , and  $K_1$  and  $K_2$  are the number of clusters in  $\rho_1$  and  $\rho_2$ , respectively. Thus, the Bayes estimator under the VI loss (called the minVI partition) is:

$$\rho^* = \min_{\rho \in \mathcal{P}} \mathbb{E} [d_{\text{VI}}(\rho, \rho') \mid \mathbf{y}] \approx \min_{\rho \in \mathcal{P}} \frac{1}{T} \sum_{t=1}^T d_{\text{VI}}(\rho, \rho^{(t)}).$$

While direct minimization cannot be performed, effective algorithms exist [Wade and Ghahramani, 2018, Rastelli and Friel, 2018, Dahl et al., 2022].

## 3 Methods

Summarizing the posterior with a single partition not only disregards uncertainty in the clustering structure, but can also be misleading in the case of multimodality (see Example 2). To address these issues, we propose to summarize with not one, but multiple optimal partitions. Our approach borrows ideas from Balocchi et al. [2023] to approximate the posterior  $\pi(\rho \mid \mathbf{y})$  with a simpler discrete distribution  $q = \sum_{\ell=1}^L w_\ell \delta_{\rho_\ell}$  supported on a small number  $L$  of partitions. Balocchi et al. focus on minimizing the Kullback-Leibler (KL) divergence and show that the optimal distribution  $q$  is supported on the set of  $L$  partitions that have largest posterior mass (for  $L = 1$ , this reduces to the MAP partition). However, such partitions tend to be very similar to each other, with only one or two points having a different cluster allocation. For example, in Figure 1b, even with the choice of  $L = 501$ , the support of  $q$  consists of the partition with a single large cluster of 500 points and all partitions with one large cluster of size 499 and one singleton. This would only summarize uncertainty around the mode, not the variability in the posterior.

Instead, we replace the KL divergence with the Wasserstein distance, which allows the use of metrics on the space of partitions. Here, we focus on the VI metric, but this can be extended to other choices. To formally define the Wasserstein-VI distance, let  $(\mathcal{P}, d_{\text{VI}})$  be the metric space on the set of partitions  $\mathcal{P}$  embedded with the VI metric  $d_{\text{VI}}$ . Let  $p$  and  $q$  represent two distributions on  $\mathcal{P}$ . If  $\mathcal{J}(p, q)$  is the set of couplings of  $p$  and  $q$ , i.e. the collection of distributions  $J(\rho, \rho')$  on  $\mathcal{P} \times \mathcal{P}$  with marginals  $p$  and  $q$  on the first and second factor respectively, then the Wasserstein distance is

$$W_{\text{VI}}(p, q) = \inf_{J \in \mathcal{J}(p, q)} \sum_{\rho, \rho' \in \mathcal{P}} d_{\text{VI}}(\rho, \rho') J(\rho, \rho').$$

Denote with  $\mathcal{Q}_L = \{\sum_{\ell=1}^L w_\ell \delta_{\rho_\ell} : \sum_{\ell=1}^L w_\ell = 1, w_\ell \geq 0, \rho_\ell \in \mathcal{P}, \text{ for } \ell = 1, \dots, L\}$  the collection of discrete distributions supported on  $L$  points.

**Definition 1.** *The WASABI posterior is the discrete distribution  $q^* = \sum_{\ell=1}^L w_\ell^* \delta_{\rho_\ell^*} \in \mathcal{Q}_L$  that best approximates the posterior in a Wasserstein-VI sense,*

$$q^* = \underset{q \in \mathcal{Q}_L}{\operatorname{argmin}} W_{VI}(\pi(\cdot|\mathbf{y}), q(\cdot)). \quad (2)$$

*The quality of the approximation is quantified by the Wasserstein-VI distance,  $W_{VI}(\pi(\cdot|\mathbf{y}), q^*(\cdot))$ , which measures minimal amount of uncertainty lost when summarizing  $L$  partitions.*

**Remark.** *In the special case of  $L = 1$ , the Wasserstein-VI distance reduces to the posterior expected VI. Thus, the optimal distribution  $q^*$  is a point mass supported on the partition  $\rho^*$  that minimizes the posterior expected VI (the minVI partition). The quality of the approximation and spread around  $\rho^*$  is quantified by the posterior expected VI of  $\rho^*$ .*

In the general case of  $L > 1$ , we can rewrite the problem of finding the WASABI posterior using properties of the Wasserstein distance between two discrete distributions (Cuturi and Doucet [2014]).

**Proposition 1.** *The WASABI posterior  $q^*$ , which is the solution to (2), is found by identifying a set of “centers” or “particles”  $\boldsymbol{\rho}^* = \{\rho_1^*, \dots, \rho_L^*\}$  that minimize*

$$\sum_{\ell=1}^L \sum_{\rho \in \mathcal{N}_\ell} d_{VI}(\rho, \rho_\ell^*) \pi(\rho|\mathbf{y}), \quad (3)$$

*where  $\mathcal{N}_\ell = \{\rho : d_{VI}(\rho, \rho_\ell^*) < d_{VI}(\rho, \rho_{\ell'}^*) \text{ for all } \ell' \neq \ell\}$  corresponds to the set of partitions that are closer to  $\rho_\ell^*$  than to any other center. We shall name  $\mathcal{N}_\ell$  the “region of attraction” of the center  $\rho_\ell^*$ . The optimal weights  $w_\ell^*$  associated to each center are found by  $w_\ell^* = \sum_{\rho \in \mathcal{N}_\ell} \pi(\rho|\mathbf{y})$ .*

In other words, the WASABI posterior is supported on the centers  $\rho_\ell^*$  that minimize (3), and the probability  $w_\ell^*$  associated with each of them is equal to the posterior mass of its region of attraction. See Appendix A for a proof of Proposition 1. In practice, even for moderate  $n$ , the objective function in (3) is intractable due to the dimension of  $\mathcal{P}$ . A similar approximation of the posterior can however be considered when an estimate of the posterior distribution is provided through MCMC samples. Let  $\hat{\pi}(\rho|\mathbf{y})$  be the approximation to the posterior provided by the MCMC draws,  $\hat{\pi}(\rho|\mathbf{y}) = \frac{1}{T} \sum_{t=1}^T \delta_{\rho^{(t)}}$ . We can then approximate  $\hat{\pi}(\rho|\mathbf{y})$  with  $q$  in a Wasserstein-VI sense.

**Definition 2.** *Given a set  $\{\rho^{(1)}, \dots, \rho^{(T)}\}$  of draws from the posterior  $\pi(\cdot|\mathbf{y})$ , the WASABI posterior is the discrete distribution  $q^* = \sum_{\ell=1}^L w_\ell^* \delta_{\rho_\ell^*} \in \mathcal{Q}_L$  that is closest in a Wasserstein-VI sense to the empirical approximation of the posterior,  $\hat{\pi}(\rho|\mathbf{y}) = \frac{1}{T} \sum_{t=1}^T \delta_{\rho^{(t)}}$ ,*

$$q^* = \underset{q \in \mathcal{Q}_L}{\operatorname{argmin}} W_{VI}(\hat{\pi}(\cdot|\mathbf{y}), q(\cdot)). \quad (4)$$

Again, thanks to the properties of the Wasserstein distance between two discrete distributions, we can find the WASABI posterior by reframing the problem as follows.

**Proposition 2.** *The WASABI posterior  $q^* \in \mathcal{Q}_L$ , which is the solution to (4), is supported on the “centers” or “particles”  $\boldsymbol{\rho}^* = \{\rho_1^*, \dots, \rho_L^*\}$  which minimize*

$$\frac{1}{T} \sum_{\ell=1}^L \sum_{\rho^{(t)} \in \hat{\mathcal{N}}_\ell} d_{VI}(\rho^{(t)}, \rho_\ell^*), \quad (5)$$

*where  $\hat{\mathcal{N}}_\ell = \{\rho^{(t)} : d_{VI}(\rho^{(t)}, \rho_\ell^*) < d_{VI}(\rho^{(t)}, \rho_{\ell'}^*) \text{ for all } \ell' \neq \ell\}$  is referred to as the “empirical region of attraction” of  $\rho_\ell^*$ . The optimal weight  $w_\ell^*$  of each  $\rho_\ell^*$  is proportional to the size of  $\hat{\mathcal{N}}_\ell$ , i.e.  $w_\ell^* = |\hat{\mathcal{N}}_\ell|/T$ .*

---

**Algorithm 1** Find the approximate WASABI posterior

---

**Input:** MCMC samples  $\{\rho^{(t)}\}_{t=1}^T$ , number of particles  $L$ , initialization method `init`, tolerance  $\epsilon$

**Initialize**  $\rho_{1:L}^*$  using method `init`

**repeat**

***N-update step:***

    Compute  $\text{VI}(\rho^{(t)}, \rho_\ell^*)$  for all  $t$  and  $\ell$

    Assign each  $\rho^{(t)}$  to the closest center  $\rho_\ell^*$ , and update the region of attraction  $\mathcal{N}_\ell$

**if** any region of attraction  $\mathcal{N}_\ell$  is empty **then**

        Replace  $\rho_\ell^*$  with a distant partition  $\rho^{(t)}$  and update  $\mathcal{N}_\ell = \{\rho^{(t)}\}$

***VI-search step:***

**for**  $\ell$  in  $1, \dots, L$  **do**

        Update centers:  $\rho_\ell^* \leftarrow \text{minVI}(\mathcal{N}_\ell)$

        Update centers' expected-VI:  $l_\ell \leftarrow \text{EVI}(\rho_\ell^*, \mathcal{N}_\ell)$

        Update weights  $w_\ell \leftarrow |\mathcal{N}_\ell|/T$

    Update loss  $W \leftarrow \sum_{\ell=1}^L w_\ell \cdot l_\ell$

**until** change of  $W$  is less than  $\epsilon$ .

**Return**  $\{\rho_1^*, \dots, \rho_L^*\}, \mathbf{w} = (w_1, \dots, w_L)$

---

As described by Canas and Rosasco [2012] and first suggested by Pollard [1982], an interesting connection arises between the k-means algorithm and the approximation in a Wasserstein sense (equipped with the Euclidean distance) of an empirical distribution with a discrete distribution supported on  $k$  points. In particular, the k-means algorithm provides a locally optimal solution to this problem. In our framework, we can obtain a locally optimal set of partitions that minimize (5) by applying a k-medoids-like algorithm, which generalizes k-means beyond the Euclidean distance, to the set of MCMC samples  $\{\rho^{(t)} : t = 1, \dots, T\}$ , with  $k = L$  and distance equal to the VI. In other words, the MCMC-sampled partitions are clustered into  $L$  groups, and each of these groups is represented by one of the centers  $\rho_\ell^*$ . These same centers are the support of the WASABI posterior  $q^*$ , with weights determined by the size of each group. While clustering a set of partitions may seem tautological, the value lies in its ability to summarize a large set of discrete objects with a much smaller number of points, each of which represents a different group or “cluster” of partitions.

**Example 1.** Consider the slightly bimodal example in Figure 1, with data generated from an equal-weight mixture of two unit-variance Gaussians (means  $\pm 1.1$ ). The *minVI* estimator identifies only one cluster, yet the posterior similarity matrix (PSM) suggests a possible two-cluster structure. Approximating the posterior with WASABI (using two particles), we find one particle corresponding to the single-cluster partition ( $w_1 \approx 0.503$ ) and another recovers two similarly-sized clusters. In this sense, WASABI is able to recover the bimodal structure of the posterior, visible in Figure 1b.

### 3.1 Algorithm

The search algorithm to find the  $L$  centers that support the WASABI posterior has a similar structure to the k-medoids algorithm. Essentially, given an initialization of the centers, the algorithm alternates between what we refer to as the *N-update* step, where the regions of attraction are updated, and the *VI-search* step, where the new center for each region of attraction corresponds to the *minVI* of each group.

More precisely, the *N-update* step assigns each point (MCMC sample) to its closest center by computing the VI distance between every point and each center. In the rare case when a partition is equally distant to multiple centers, it is randomly assigned. Computing VI distances between all points and centers has complexity  $O(nTL)$ .

Next, the *VI-search* updates the center of each group given their new region of attraction, but unlike k-medoids, which restricts the search to the points within the group, we make use of more advanced algorithms to minimize the posterior expected VI, such as SALSO [Dahl et al., 2022]. The

complexity of this step depends on the algorithm selected, e.g. for SALSO (the default), the cost is  $O(nTK_{\max}^2)$ , where  $K_{\max}$  is the maximum number of clusters considered in the search algorithm.

The algorithm iterates between these steps until a maximum number of iterations is reached, or the improvement in the Wasserstein distance is less than a given threshold  $\epsilon$ . Since the VI distance is bounded above by  $\log_2(n)$ , we recommend choosing a threshold based on this, such as  $\epsilon = 0.0001 * \log_2(n)$ . The basic algorithm is outlined in Algorithm1, and a more detailed version is in SectionB of the Appendix. As the algorithm only guarantees convergence to a local optimum, we recommend running it multiple times with different starting conditions. We consider several initialization strategies, including using the top  $L$  partitions found with hierarchical clustering based on the PSM, or a strategy mimicking k-means++ initialization [Vassilvitskii and Arthur, 2006], which randomly initializes centers by selecting more spread out partitions among the samples. (Appendix, SectionB). To reduce computational complexity, strategies used in k-means can be adapted; for example, we allow a “mini-batch” option, where at each iteration, we consider a subsample of the MCMC partitions of size  $B$ . This reduces the cost to  $O(nB(L + K_{\max}^2))$  but is followed by a small number of iterations using the full set of MCMC partitions, similar to the two-stage k-means of Salman et al. [2011].

**Choosing the number of particles  $L$**  To approximate the posterior distribution with WASABI, the practitioner must select the number of particles  $L$ . As  $L \rightarrow T$ , the Wasserstein distance reduces to zero, but it becomes more difficult to describe all centers. To achieve a balance between parsimony (small  $L$ ) and a good enough approximation (small Wasserstein distance), we propose running the algorithm for a range of values of  $L$  (usually from 1 to 10), and plotting the Wasserstein distance as a function of  $L$ . This produces an “elbow plot”, and the selected value of  $L$  is the smallest that corresponds to a significant reduction of the Wasserstein distance, before the curve flattens (or decreases less substantially). See e.g. Figure 2c.

### 3.2 Describing and visualizing the particles

Clustering is often used for exploratory data analysis, and visualization of the partitions is a crucial part of the analysis to uncover patterns in the data. Similarly, visualization of the obtained particles is essential to better understand the structure of the posterior distribution. For the slightly bimodal data (Example 1), comparison of the particles is straightforward. We now consider a two-dimensional extension of this simple example, and in the following, outline several techniques to describe and visualize the particles that summarize the posterior, illustrated on this two-dimensional example.

**Example 2.** *Consider a two-dimensional Gaussian mixture with four components, each with mean  $(\pm m, \pm m)$  located in one of the four quadrants and diagonal covariance matrix with unit variance. Figure 2a displays the data colored by the partition used in the data-generating process (for  $m = 1.25$ ). MCMC samples are obtained by fitting a diagonal location-scale Dirichlet process mixture (DPM) using the BNPmix R package [Corradin et al., 2021]. The minVI partition (Figure 2b) merges three of the four components, which does not reflect the axis-aligned elliptical clusters of the DPM model. This highlights that a single-point estimate can be misleading when the posterior is multimodal. In fact, the WASABI elbow plot (Figure 2c) suggests that multiple estimators are useful for describing the posterior. We now provide several approaches for visualizing the WASABI particles.*

**Weight and number of clusters for each particle** Determining the number of clusters is an important problem, and with WASABI, we can compare the number of clusters identified by the different particles. In several experiments, we have found that different particles often tend to have different numbers of clusters. Moreover, the weights associated with the particles convey their importance in summarizing the posterior MCMC samples, as they correspond to the proportion of samples that are closer to each given particle. See the left panel of Figure 1d for a representation of these quantities for Example 1.

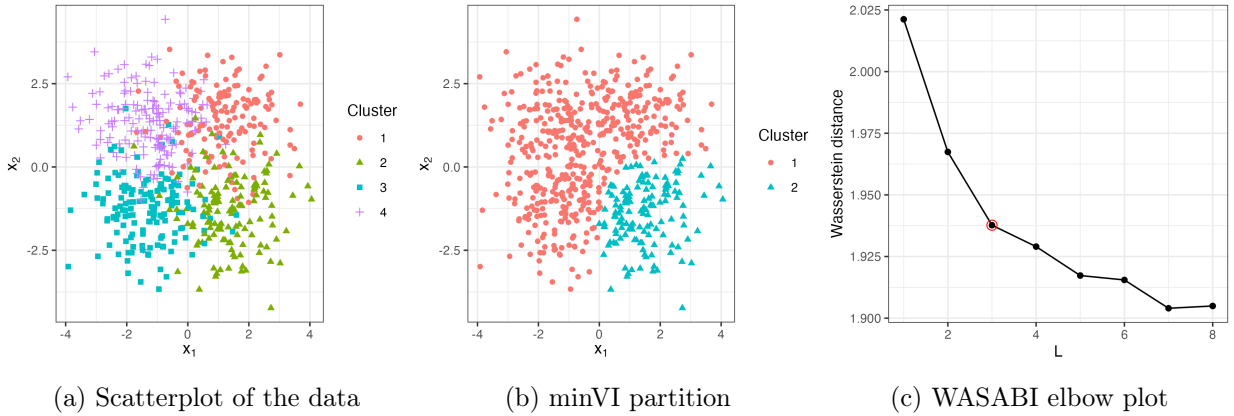


Figure 2: Two-dimensional extension of the bimodal example. Data is generated from a Gaussian mixture with four components (Panel 2a). The minVI merges three components (Panel 2b). To choose the number of particles  $L$  in WASABI, we construct an elbow plot (Panel 2c) which suggests  $L = 3$  particles achieves a balance between parsimony and minimizing the objective.

**Visualizing particles, with the data colored by cluster membership** The number of clusters provides limited information on the partition itself. By visualizing the partition corresponding to each particle, side by side, and depicting the data points colored by their cluster allocation, we can identify how the clusters change. For data that is more than 2-dimensional, transformations can be applied, such as principal component analysis.

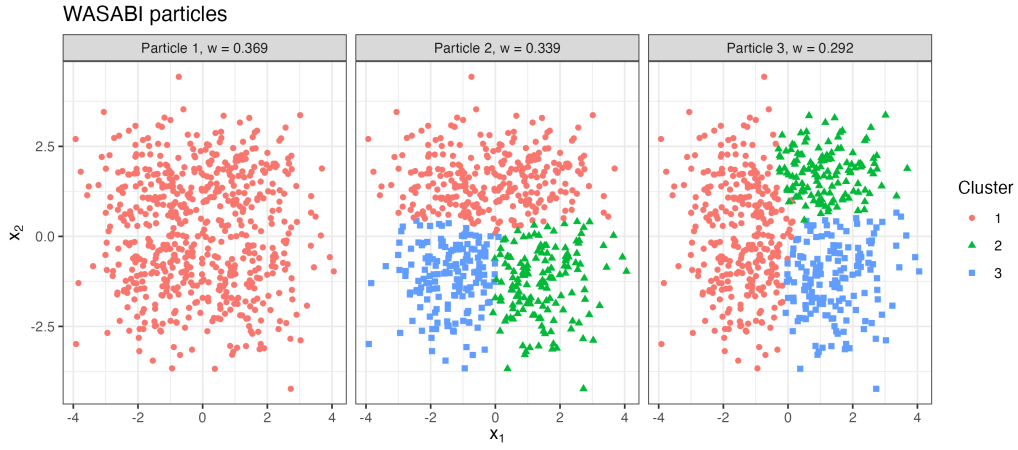
**Example 2** (continued). *Figure 3a displays the partitions recovered by each of the particles. The second particle detects three clusters, merging together the two top ‘true’ components, while the third one recovers again three clusters, merging together the two left ‘true’ components. Notice how the minVI partition is not among the particles and is obtained as product of the multimodality and uncertainty in merging either the two top components (particle 2) or the two left components (particle 3). Additionally, unlike Example 1, the particles are not nested within each other and could not be recovered using a hierarchical clustering method.*

**Comparing the particles globally: visualizing the meet** For a global comparison of the particles, we can examine their *meet*. In the space of partitions, which forms a partially ordered set under the relation of set containment, the meet (denoted  $\wedge$ ) corresponds to the *greatest lower bound* of a collection of partitions. Specifically, the meet of a set of partitions is the coarsest partition such that each of its clusters is fully contained within a cluster of every partition in the set. The meet’s clusters highlight which data points are always clustered together across all of the partitions from the set. Therefore, by visualizing the particles’ meet we can better identify parts of the data points that are consistently clustered together in WASABI.

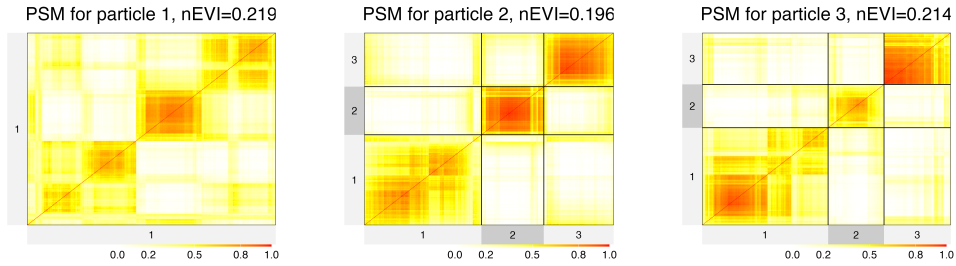
**Example 2** (continued). *Figure 3c (top) shows the cluster allocation of the meet partition of the particles. The four largest clusters recover the four quadrants that correspond to the four components used to generate the data, while the three remaining clusters corresponds to a small number of data points whose cluster assignment changes in particles 2 and 3. For example, the data points in meet cluster 5 were allocated in cluster 1 in particle 2 and in cluster 3 in particle 3.*

**Comparing pairs of particles: the VI-contribution** Sometimes, the visualization of particles side by side does not allow for a full understanding of the differences in the cluster assignment, especially when the number of data points is large. Instead, we can highlight the differences between two particles by considering each point’s contribution to the VI distance between those particles.

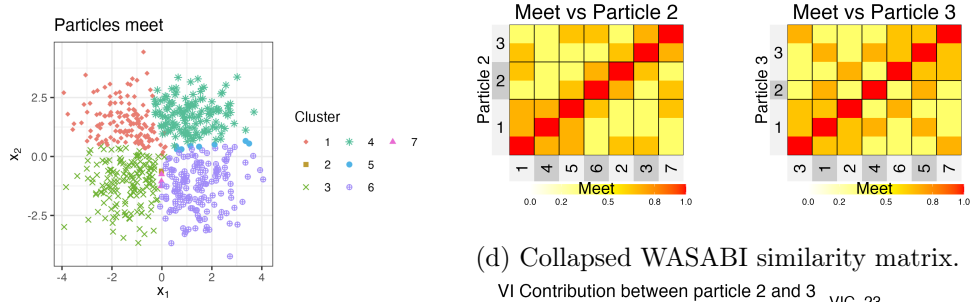
**Definition 3** (VI contribution). *The VI distance between two partitions  $\rho_1$  and  $\rho_2$  can be written as the sum over all data points of a non-negative contribution,  $VI(\rho_1, \rho_2) = \sum_{i=1}^n VIC_i(\rho_1, \rho_2)$ , where each*



(a) Data colored by particles' cluster assignment.



(b) Posterior similarity matrix (PSM) for each particle's region of attraction.



(c) Cluster allocation and EVIC for the particles' meet.

(d) Collapsed WASABI similarity matrix.

(e) VIC between particle 2 and particle 3.

Figure 3: Several possible visualizations of the WASABI summary for Example 2: (a) scatterplot of the data colored by particles' cluster assignment, (b) posterior similarity matrix for the samples within each region of attraction, (c) the particles' meet, (d) posterior similarity matrix using the WASABI approximation collapsed to meet's clusters, (e) comparison of two particles using VI contribution.

point's contribution to the VI is defined as

$$VIC_i(\rho_1, \rho_2) = \frac{1}{n} \left[ \log_2 \left( \sum_{i'=1}^n \frac{\mathbf{1}(c_{1,i} = c_{1,i'})}{n} \right) + \log_2 \left( \sum_{i'=1}^n \frac{\mathbf{1}(c_{2,i} = c_{2,i'})}{n} \right) - 2 \log_2 \left( \sum_{i'=1}^n \frac{\mathbf{1}(c_{1,i} = c_{1,i'}, c_{2,i} = c_{2,i'})}{n} \right) \right].$$

Note first that if two points are clustered together under the meet  $\rho_1 \wedge \rho_2$ , then their VI contribution will be the same. Moreover, the VI contribution will be zero for a point only if it is clustered with the same set of points in both partitions. More precisely, if a cluster  $C_h \in \rho_1$  and  $C_h \in \rho_2$  (and consequently  $C_h \in \rho_1 \wedge \rho_2$ ), then  $\text{VIC}_i(\rho_1, \rho_2) = 0$  for any  $i \in C_h$ . At the other extreme, if a data point is clustered with a completely different set of data points, then its VI contribution will be large, especially if the respective clusters are large, i.e. if  $i \in C_{h_1}$  in  $\rho_1$  and  $i \in C_{h_2}$  in  $\rho_2$ , and  $|C_{h_1} \cap C_{h_2}| = 1$ , then  $\text{VIC}_i(\rho_1, \rho_2) = (\log_2(n_{h_1}) + \log_2(n_{h_2}))/n$ . A full derivation of the VI contribution is included in Appendix C.1.

**Example 2** (continued). *Coloring the data points based on their VI-contribution can help pinpoint areas within the dataset where the two particles differ, enabling more detailed investigation. Figure 3e compares particles 2 and 3, with the lowest VI contribution for the bottom right quadrant, highlighting that these points are mostly clustered together, and the highest for points on the border, suggesting more drastic changes in who they are clustered with.*

Since the VI contribution is constant for all points in the same meet cluster, we can define the “VI contribution by group” (VICG), i.e. the aggregate VIC for all points in the same meet cluster.

**Definition 4** (VI contribution by group). *The VI distance between the two partitions can be written as the sum over all clusters in the meet of a non-negative “group contribution”,  $\text{VI}(\rho_1, \rho_2) = \sum_{k_1=1}^{K_1} \sum_{k_2=1}^{K_2} \text{VICG}_{k_1, k_2}(\rho_1, \rho_2)$ , where*

$$\text{VICG}_k(\rho_1, \rho_2) = \frac{n_{k_1, k_2}}{n} \left[ \log_2 \left( \frac{n_{k_1, +}}{n} \right) + \log_2 \left( \frac{n_{+, k_2}}{n} \right) - 2 \log_2 \left( \frac{n_{k_1, k_2}}{n} \right) \right].$$

The “groups” of the VI contribution by group correspond to the meet’s clusters, which are also found as the pairwise intersection of each of the particles’ clusters. While inspecting the VIC for each data point highlights the subtle differences between two partitions, plotting the VICG highlights high-level changes in the two partitions. In fact, major changes in the cluster assignment, such as a large cluster being split into two equally-sized subclusters, would have a significant contribution to the VI, but if the number of points in those clusters is large, the individual contribution may be negligible, since each point is still clustered together with many of the same points. However, by aggregating the contribution across all points in the meet’s cluster in the VICG, these large-scale differences become more visible. Figure 11 in the Appendix displays the VICG for Example 2.

**Investigating the co-clustering properties of the meet’s clusters** When the number of clusters in the particles’ meet is large, we can benefit from a better understanding of how often these clusters are combined together across the particles. The proposed visualization achieves this, while also comparing the meet with each of the particles. Specifically, for any pair of meet clusters  $C_k, C_h \in \bigwedge_{\ell=1}^L \rho_\ell^*$ , we consider their WASABI posterior similarity, defined as the posterior probability that any two points in these meet clusters,  $i \in C_k$  and  $i' \in C_h$ , are clustered together as approximated by WASABI,  $\Pr(c_i = c_{i'} | \mathbf{y}) \approx \sum_{\ell=1}^L w_\ell \mathbb{1}(\{C_k \cup C_h\} \in \rho_\ell^*)$ . In other words, we measure how often the meet’s clusters are clustered together in the particles using their weights. This is equivalent to using WASABI to approximate the posterior similarity matrix, grouped by the meet’s clusters (instead of individual data points, since it will be equal among points with the same allocation in the meet). We can visualize this PSM by grouping together the meet’s clusters that form each of the clusters in a particle, and thus providing further investigation in the particle’s structure. See for example Figure 3d for a comparison of particles 2 and 3 with the meet, for Example 2. The meet’s clusters are aggregated within the particle’s clusters in the rows, with labels shown on the left margin.

**Determining uncertainty in each region of attraction: inspecting each particle’s PSM**

The WASABI particles summarize the posterior with several “point estimates” that can be visualized for easy understanding of the posterior structure. Uncertainty remains around each of the particles, as they are the representative partition for a group of MCMC samples (their “region of attraction”). To understand the uncertainty in each region of attraction, we can visualize the PSM of each region, i.e. calculating it only using the MCMC samples that are closest to the corresponding particle. For

example, Figure 3b displays the PSM for each particle’s region of attraction for Example 2, using heatmaps that group points by their cluster assignment. Additionally, for each particle, we compute the (normalized) expected VI restricted to its region of attraction, i.e. approximated using only MCMC samples in its region of attraction. This quantifies the spread of the samples around the particle; for example, there is more variability in the first region of attraction (characterized by a single, large cluster) compared to the second (see plot titles in Figure 3b). For an alternative visualization that groups data points by the meet clusters, see Figure 9 of the Appendix.

### Determining uncertainty in each point’s cluster allocation: the expected VI contribution

While the VIC enables the comparison of two specific partitions, the same decomposition of the VI can also be applied in the context of the expected VI to obtain a measure of uncertainty in each point’s cluster allocation. Essentially, the expected VI quantifies the variability of the posterior around a particular partition. By analyzing how each point contributes to the EVI, we can derive a measure of uncertainty for the cluster assignment of each point.

Let  $\rho^*$  be an estimator for a partition (such as the minVI, or one of the WASABI particles). We define the contribution of the  $i$ th data point to the expected VI of  $\rho^*$  in Definition 5.

**Definition 5** (EVI contribution). *The contribution of the  $i$ th data point to the EVI of  $\rho^*$  is*

$$EVIC_i(\rho^*) = \frac{1}{n} \left\{ \log_2 \left( \sum_{i'=1}^n \frac{\mathbf{1}(c_i^* = c_{i'}^*)}{n} \right) + \mathbb{E} \left[ \log_2 \left( \sum_{i'=1}^n \frac{\mathbf{1}(c_i = c_{i'})}{n} \right) \mid \mathbf{y} \right] - 2\mathbb{E} \left[ \log_2 \left( \sum_{i'=1}^n \frac{\mathbf{1}(c_i^* = c_{i'}^*, c_i = c_{i'})}{n} \right) \mid \mathbf{y} \right] \right\},$$

where the expectation is taken with respect to  $\pi(\rho \mid \mathbf{y})$ , the posterior distribution over the space of clusterings. The EVI of  $\rho^*$  is  $EVI(\rho^*) = \sum_{i=1}^n EVIC_i(\rho^*)$ .

Note that computing the contribution of the  $i$ th data point the EVI of  $\rho^*$  requires computing the expectation with respect to the posterior over the space of partitions. This can be approximated either based on the MCMC draws or the WASABI posterior (Section C.1 of the Appendix). The latter has a clear computational advantage ( $O(nL)$  as opposed to  $O(nT)$  with  $L \ll T$ ); in addition, note that when  $\rho^*$  is one of the particles, every data point in the same cluster of the meet will have the same contribution to the EVI, further reducing computations and enhancing interpretation. For example, clusters in the meet with a WASABI approximated EVI of zero, are always clustered together and never with any other data points, across all particles. Lastly, we note that the EVI of the  $l$ th particle,  $\rho_l^*$ , can also be taken with respect to the posterior restricted to its region of attraction to shed light on which points are more uncertain (or stable) in their cluster allocation within the region of attraction.

**Example 2** (continued). *The contribution to the EVI for the meet of the particles is displayed in Figure 3c (bottom). By analyzing the patterns in this figure, we notice that the points with the largest EVIC are the ones at the border between the four large clusters (depicted in Figure 3c (top) and represented here with different shapes). Moreover, the points in the top-left component (labeled with 1) have a slightly larger EVIC than the points in the bottom-right component (labeled with 6), reflecting that their cluster allocation changes more across the MCMC samples, while the cluster assignment of the points in cluster 6 change less.*

## 4 Experiments

We now consider several simulated datasets to illustrate scenarios when WASABI can be beneficial in explaining the uncertainty in the posterior. We consider two main settings: (1) the model is correctly specified, but the mixture components are not well-separated, and (2) the model is misspecified.

First, we consider scenario (1), by examining different levels of cluster separation in Example 2. Specifically, several values of  $m$ , defining the means ( $\pm m, \pm m$ ) of the four mixture components, are considered (see Figure 14 in the Appendix). For each value of  $m$ , we generate 10 datasets. When

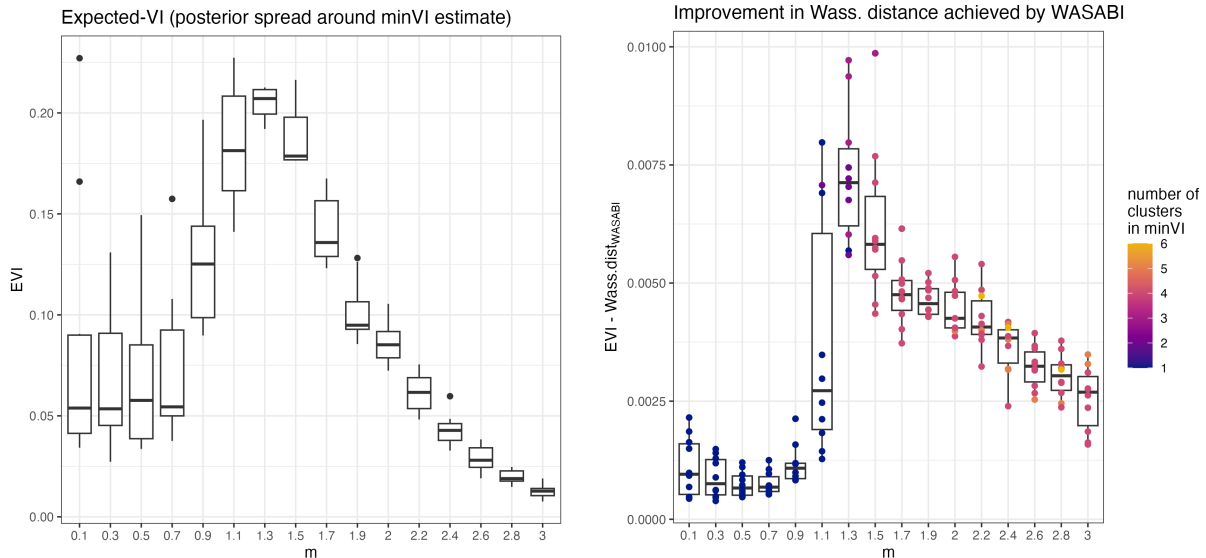


Figure 4: Experiment with different levels of cluster separation, determined by  $m$ . Left panel: posterior spread around the minVI estimator, quantified by its EVI. Right panel: improvement in Wasserstein distance achieved by WASABI for different values of  $m$ ; the points are colored by the number of clusters in the corresponding minVI estimate.

$m$  is small, the four components overlap, making the posterior concentrated around the partition with one cluster. Instead, when  $m$  is large, the four components are well separated and easy to distinguish.

To quantify the uncertainty in the posterior, we measure the spread around its center by the EVI. This is displayed in the left panel of Figure 4, showing how the posterior uncertainty starts low and increases when there is a moderate level of cluster separation, and then decreases when the cluster separation is high. The right panel of Figure 4 instead shows the improvement in the Wasserstein distance achieved by WASABI, quantified by  $\text{EVI}(\rho^*) - W_{\text{VI}}(\hat{\pi}, q^*)$ , when summarizing with  $L = 10$  particles instead of a single estimator. These figures show that WASABI explains the variation in the posterior the most when the posterior uncertainty is highest (i.e. for values of  $m \approx 1.3$ ).

In scenario (2), we explore several examples of misspecified models with data generated from different distributions: (a) a bivariate Gaussian distribution truncated to the unit square, and (b) a bivariate skewed-t distribution (assuming independence). To investigate the effect of misspecification, in (a), the standard deviation is varied, so that small values are well-specified and larger values resemble a uniform distribution on the unit square; and in (b), the degrees of freedom and skewness parameter are varied. A detailed description of these experiments is in Section D.2 of the Appendix.

Figure 5 displays the improvement in Wasserstein distance achieved by WASABI as a function of the posterior spread (measured by EVI) for (a) the truncated Gaussian distribution (top row, left panel), and (b) for the skewed-t distribution with  $df = 5$  (second row, left panel). Overall, WASABI tends to explain higher variations in the posterior when the EVI is larger. This also correlates with increasing misspecification; for the truncated Gaussian distribution (a), the EVI increases with the standard deviation, and for the skewed-t distribution with  $df = 5$  (b), larger values of the skewness parameter result in higher EVI. The same improvement is visible in the bottom row (all panels) for the skewed-t distribution with varying degrees of freedom, where we also observe that most of the variation is driven by the skewness parameter, but for smaller degrees of freedom, higher posterior uncertainty (and improvement by WASABI) is observed. Finally, the central and right panels in the first two rows illustrate the WASABI results for one example, with median EVI value, corresponding to  $\sigma = 0.4$  for the truncated Gaussian, and to  $df = 5$  and skewness of 2 for the skewed-t.

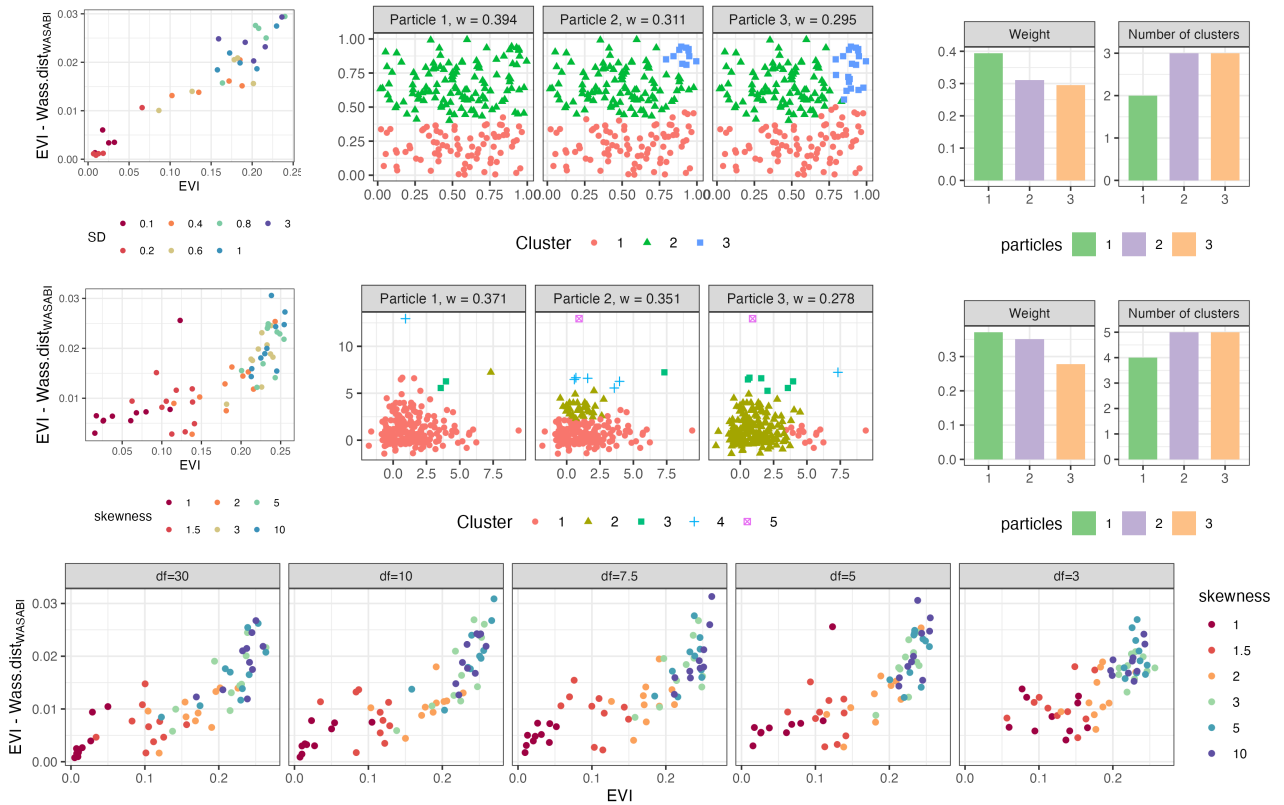


Figure 5: Experiment with misspecified models. The top two rows show results for truncated Gaussian and skewed- $t$  ( $df = 5$ ) distributions. *Left*: improvement in Wasserstein distance by WASABI versus posterior spread (EVI); *central/right*: particle scatterplots with cluster assignments and a summary plot, for one simulated dataset. The bottom row shows Wasserstein improvement for the skewed- $t$  with varying degrees of freedom.

## 5 Real data analysis

### 5.1 Effects of neighborhood deprivation on HPV vaccine uptake

The human papillomavirus (HPV) vaccine, a key tool in reducing cervical and other cancers, is routinely offered to 14-year-old girls in Scotland. However, decline in uptake is a global concern, underscoring the need to examine factors that influence this pattern. Here, we focus on studying how neighborhood deprivation may affect HPV vaccine uptake in Scotland. The data<sup>1</sup> consists of the percentage of HPV uptake, denoted by  $y_i$ , and the deprivation level, denoted by  $x_i$  and measured as the proportion of young people living in the most income deprived quintile, across the  $n = 1279$  Scottish Intermediate Zones. The left panel of Figure 6 visualizes HPV uptake across these zones.

Simple linear regression models only allow us to understand how deprivation affects mean uptake. Importantly, we are also interested in the left tail of relatively low uptake and how it is influenced by deprivation. This motivates the use of models for *density regression*, which allow the entire density of HPV uptake to change as a function of deprivation. We focus on Bayesian dependent mixtures [Wade and Inácio, 2025], which allow flexible density regression and are validated by well-established theory [Ghosal and Van der Vaart, 2017]. In particular, we employ a Bayesian mixture of linear regressions [Rodríguez-Álvarez et al., 2025], assuming  $Y_i|x_i \sim \sum_{k=1}^{\infty} w_k N(\alpha_k + \beta_k x_i, \sigma_k^2)$ , where the weights have a stick-breaking construction  $w_k = v_k \prod_{j < k} (1 - v_j)$  and  $v_k \sim \text{Beta}(1, \alpha)$ . MCMC is used to approximate the posterior distribution and estimate the conditional densities of vaccine uptake given different levels of neighborhood deprivation (center panel of Figure 6). There is a tail of regions with less uptake, which is more present as deprivation increases. To better understand this behavior and the underlying regions, WASABI can be used to summarize the MCMC draws of clusterings associated to the Bayesian

<sup>1</sup>Data available through Public Health Scotland: [https://scotland.shinyapps.io/ScotPHO\\_profiles\\_tool/](https://scotland.shinyapps.io/ScotPHO_profiles_tool/)

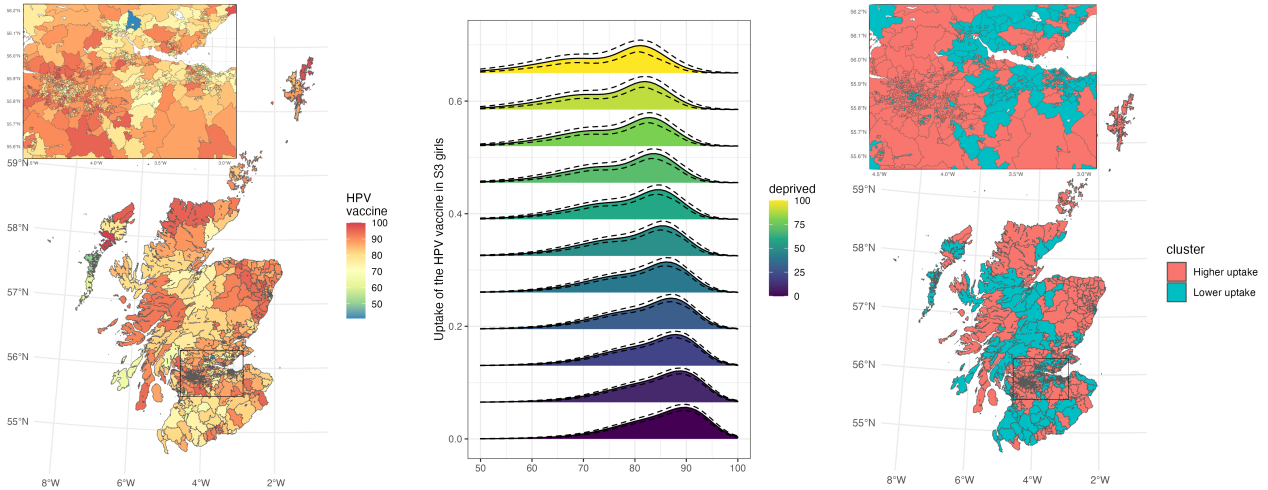


Figure 6: HPV vaccine uptake in Scotland. *Left*: Visualization of HPV uptake rates across neighborhoods. *Center*: Estimated conditional density (with pointwise credible intervals) of HPV vaccine uptake by neighborhood deprivation, showing lower uptake and a bimodal pattern for higher deprivation neighborhoods. *Right*: Map of the second WASABI particle’s cluster assignments.

mixture model.

The posterior on the clustering structure reflects groups of neighborhoods with similar relation between uptake and deprivation and overall level of uptake. To summarize and understand this posterior, WASABI finds two particles with weights  $w_1 = 0.87$  and  $w_2 = 0.13$ ; the first particle corresponds to the partition with one cluster, while the second one finds two clusters. This reflects the possibility of two groups of regions with different patterns, although the separation is not clear. The two clusters of the second particle (depicted in the right panel of Figure 6) are characterized by the two linear regression equations, respectively  $(\hat{\alpha}_1, \hat{\beta}_1) = (90.05, -0.09)$  for the higher uptake cluster and  $(\hat{\alpha}_2, \hat{\beta}_2) = (76.18, -0.12)$  for the lower uptake cluster, whose lower uptake becomes even more pronounced as deprivation decreases. Interestingly, from the map of the second particle (right panel of Figure 6), we can see a spatial correlation in the cluster assignments, and that surprisingly the two main cities in Scotland, Edinburgh and Glasgow, have very different patterns. Edinburgh seems to be comprised mostly of lower-uptake regions, while Glasgow of higher-uptake regions. Further investigations are required to understand this difference, possibly caused by factors, such as high school catchments, the effect of word-of-mouth, and local advertisement and health facilities.

## 5.2 Investigating projection patterns at the single-neuron resolution

Mapping long-range connectivity in the brain is crucial to establish biological mechanisms of cognition and understand brain dysfunction in disorders. Recent technology [e.g. Keschull et al., 2016, Chen et al., 2019] allows mapping axonal projections at the level of individual neurons by tagging thousands of neurons in parallel with unique mRNA barcodes and employing sequencing of tissues biopsies at target areas. Since the RNA is transported to the axon terminals, the observed barcode counts for each neuron reflect the relative strength of projection to the target areas. Compared with bulk-labeling technologies, this has revealed unexpected diversity in projection patterns among otherwise similar neurons. To disentangle this heterogeneity, a novel statistical method for barcode counts [HBMAP, Wade et al., 2025] employs hierarchical Bayesian mixtures to identify projection patterns and integrate data across multiple experiments.

We consider data from Chen et al. [2019] measuring projections from the auditory cortex to the 11 target regions (the orbitofrontal cortex (OFC), motor cortex (Motor), rostral striatum (Rstr), somatosensory cortex (SSctx), caudal striatum (Cstr), amygdala (Amyg), ipsilateral visual cortex (VisIp), contralateral visual cortex (VisC), contralateral auditory cortex (AudC), thalamus (Thal), and tectum (Tect)) for two brains using BARseq [Barcoded Anatomy Resolved by Sequencing, Chen et al., 2019], with 605 and 704 neurons observed for each brain. To summarize the MCMC samples

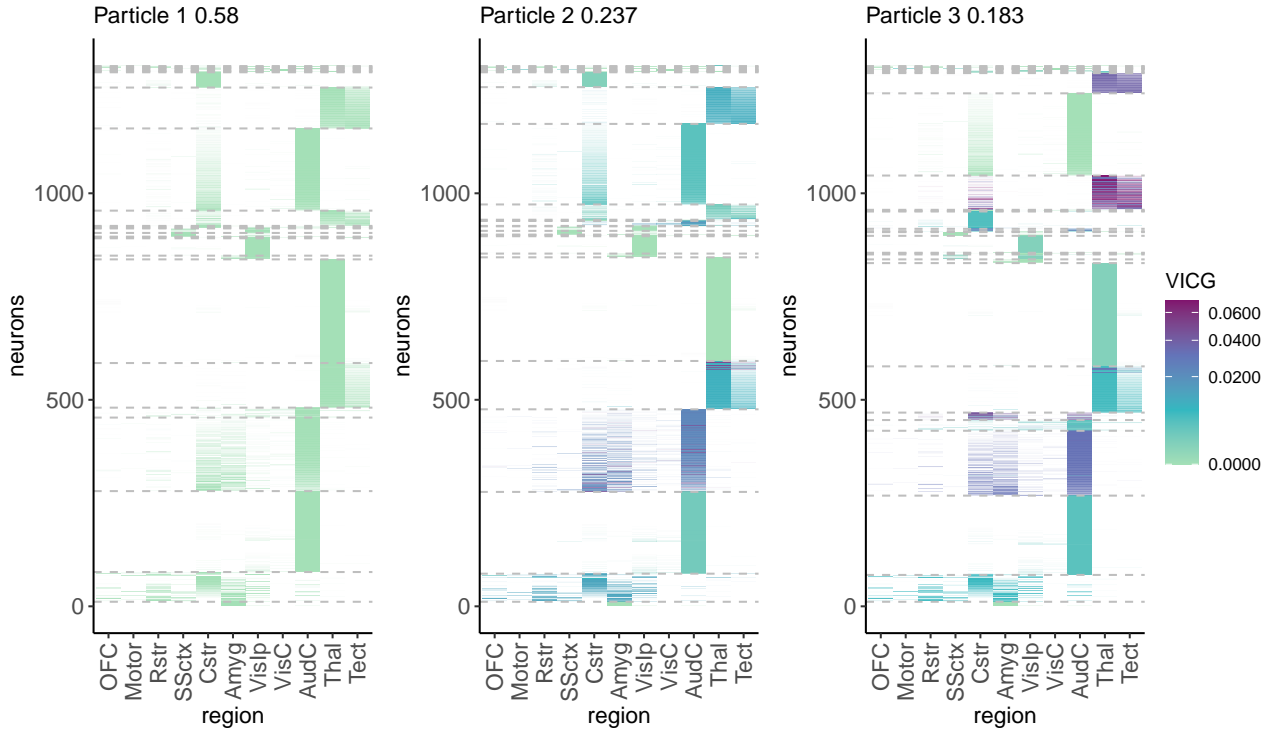


Figure 7: Summarizing uncertainty in projection patterns from the auditory cortex. The empirical projection strength (computed as the neuron’s barcode counts divided by its total count) for each neuron (row) across the 11 target areas (columns) is illustrated by transparency. Each panel depicts the clustering of a particle, with neurons belonging to different clusters separated by dashed lines. Neurons are colored by their VIC by group comparing each particle to the first particle, to understand global differences in clustering across particles.

of partitions from HBMAP, the  $L = 3$  particles of WASABI contain between 18 and 22 clusters (further details in Section E.1 of the Appendix). The clustering and projection patterns (referred to as projection motifs in the literature) identified by each particle are illustrated in Figure 7; dashed lines identify the clusters of neurons, and transparency reflects empirical projection strength (normalized barcode counts). To understand global differences between particles, neurons are colored by their group contribution to the VI distance between the first particle and each subsequent particle. We find that WASABI identifies a number of distinct projection motifs that are stable across the particles, particularly those characterizing projection to a single target area, such as the groups of neurons projecting only to Thal, Amyg, or Vislp. On the other hand, other motifs show more uncertainty, specifically, those characterizing more broad projections to two or more areas. For example, consider the group with high projection strength to AudC and low strength to Cstr and Amyg in particle 1. In particle 2, it is merged with another group of neurons with high strength to AudC and low strength to other areas in the ipsilateral cortex; instead, in particle 3, it is further split based on neurons with relatively lower strength to AudC. Another example is provided by neurons projecting to both Thal and Tect; these clusters are regrouped across the particles depending on their relative strength to these regions and if they exhibit low strength to Cstr. Overall, WASABI finds a number of distinct projection motifs from the auditory cortex, but some may have overlap or be further separated or merged, particularly those projecting more broadly across more than one target area.

## 6 Discussion

Interpreting uncertainty characterized by the posterior distribution is challenging in complex, high-dimensional Bayesian models. As the posterior is intractable in such models, algorithms for approximate inference, such as MCMC, are employed, which return tens of thousands of approximate posterior

draws. In this work, we focus on clustering, where the posterior is defined on the high-dimensional, partially-ordered space of partitions. In this non-standard setting, we propose a Wasserstein Approximation for Bayesian clustering (WASABI) to summarize the posterior draws with a small number of weighted partition estimates. Through extensive simulations and analyses, we showcase its utility in practical cases when some clusters are not well separated or the model may be misspecified. Indeed, we demonstrate how focusing on a single clustering estimate can be misleading in such cases and how WASABI captures the different modes of clustering.

The Wasserstein approximation requires selecting a metric on the partition space. We focus on the variation of information [Meilă, 2007], also exploiting its properties to propose novel tools to assess uncertainty in the cluster assignment of individual points. However, WASABI can be extended to other choices, such as Binder’s loss, ARI, or generalizations [Dahl et al., 2022], or to more general settings, e.g. Buch et al. [2024] develop a Bayesian approach to clustering in the presence of noise.

An efficient algorithm, along with various tools to visualize and quantify uncertainty, is provided in the R package at <https://github.com/cecilia-balocchi/WASABI>. In practice, only a small number of iterations are typically required, with each one scaling linearly with the number of data points and MCMC samples. To reduce the cost of the latter, WASABI allows subsampling of the MCMC draws. For the former, future work will explore combining WASABI with distributed methods [Ni et al., 2020].

WASABI is useful for improved interpretation of the posterior, but could also be relevant for posterior compression in order to reduce both storage (saving only the WASABI particles and weights) and the computational cost of predictive inference. For example, density estimation can be expensive, depending on the size of the grid or number of new locations. For Example 1, density estimates are provided in Section D.3 of the Appendix, where the WASABI-based estimates significantly reduce the cost by a factor of 1,000 compared to MCMC, at only a small increase in error.

Beyond clustering, the Wasserstein approximation could be beneficial for other Bayesian models. Future work will investigate settings, such as variable selection, trees, networks, and more.

## Appendix

### A Proof to Proposition 1

*Proof.* Let  $\mathbf{w}^* = (w_1^*, \dots, w_L^*)$  and  $\boldsymbol{\rho}^* = \{\rho_1^*, \dots, \rho_L^*\}$  respectively denote the vector of weights and the set of atoms of  $q^*(\cdot) = \sum_{\ell=1}^L w_\ell^* \delta_{\rho_\ell^*}(\cdot)$ . To solve eq. (2) we need to find the optimal  $\mathbf{w}^*$  and  $\boldsymbol{\rho}^*$ , but also for a given  $q$  we need to find the optimal coupling  $J^*(q)$  that minimizes  $\sum_{\rho, \rho'} d_{VI}(\rho, \rho') J(\rho, \rho')$  and that satisfies the marginal constraints.

Note that we can equivalently frame the problem as finding the optimal set of atoms  $\boldsymbol{\rho}^*$  and the optimal  $J^*$  such that  $\sum_{\rho} \sum_{\ell=1}^L d_{VI}(\rho, \rho_\ell^*) J^*(\rho, \rho_\ell^*)$  is minimized and  $\sum_{\ell=1}^L J^*(\rho, \rho_\ell^*) = \pi(\rho|\mathbf{y})$ . From  $J^*$  we can recover the set of weights  $\mathbf{w}^*$  as  $w_\ell^* = \sum_{\rho} J^*(\rho, \rho_\ell^*)$  for  $\ell = 1, \dots, L$ .

This follows from the fact that, for any  $J$  and for each  $\rho, \rho_\ell^*$ , we have that  $J(\rho, \rho_\ell^*) \leq \pi(\rho|\mathbf{y})$ ; this means that  $w_\ell^* = \sum_{\rho} J^*(\rho, \rho_\ell^*) \leq \sum_{\rho} \pi(\rho|\mathbf{y}) \leq 1$  and that  $\sum_{\ell=1}^L w_\ell^* = \sum_{\ell=1}^L \sum_{\rho} J^*(\rho, \rho_\ell^*) = \sum_{\rho} \sum_{\ell=1}^L J^*(\rho, \rho_\ell^*) = \sum_{\rho} \pi(\rho|\mathbf{y}) = 1$ .

To find the optimal  $J^*$  given  $\boldsymbol{\rho}^*$ , note that we can find the values  $J^*(\rho, \rho_\ell^*)$  independently for each  $\rho$ . Thus for each  $\rho$  we can recover these values by minimizing  $\sum_{\ell=1}^L d_{VI}(\rho, \rho_\ell) J^*(\rho, \rho_\ell)$  over  $(J^*(\rho, \rho_\ell^*))_{\ell=1}^L$  with the constraint that  $\sum_{\ell=1}^L J^*(\rho, \rho_\ell^*) = \pi(\rho|\mathbf{y})$ . This can be recognized as a linear program, which is solved by  $J^*(\rho, \rho_\ell^*) = \pi(\rho|\mathbf{y})$  for  $\ell = \ell^*(\rho)$ , where  $\ell^*(\rho) = \operatorname{argmin}_{\ell} d_{VI}(\rho, \rho_\ell)$ , and  $J^*(\rho, \rho_\ell^*) = 0$  for  $\ell \neq \ell^*(\rho)$ . Note that in the case where there are multiple  $\rho_\ell^*$  minimizing the VI distance with  $\rho$ , then a continuum of solutions exists; we focus on the extreme cases of allocating  $\rho$  to all equally distant particles and consider all possible solutions. This can be done in practice by randomly allocating  $\rho$  to one of the closest particles  $\rho_\ell^*$ , and setting  $J^*(\rho, \rho_\ell^*) = \pi(\rho|\mathbf{y})$ .  $\square$

## B Detailed algorithm and initialization strategies

The algorithm to find the approximate WASABI posterior (see Section 3.1) is akin to the k-medoids approach and only guarantees convergence to a local optimum. Therefore, it is standard practice to run the algorithm multiple times with different initializations, to increase the chance of finding a better (lower-loss) solution. Below, we describe in detail the initialization strategies implemented:

- *Average Linkage Initialization*: A hierarchical clustering is performed on the posterior similarity matrix using average linkage, and the tree is cut from one to a maximum number of clusters, `K.max` (by default `K.max` is set to maximum number of clusters across the MCMC samples plus 10). Among these solutions, the  $L$  particles are initialized by those with the lowest EVI. This approach specifies the initialization with each particle containing a unique number of clusters. The computational cost is  $O(n^2 \log(n) + TnK.max)$ , with the first term representing the cost of hierarchical clustering and the second corresponding to the cost of computing the EVI for the `K.max` candidate partitions. A thinning parameter can be specified to reduce the cost of this second term (defaults to 10). Note that this requires the user to pass in the pre-computed posterior similarity matrix, with computational complexity  $O(n^2T)$  and storage cost of  $O(n^2)$ .
- *Complete Linkage Initialization*: Analogous to average linkage initialization, but with complete linkage.
- *k-means++ style Initialization (++)*: Analogous to the k-means++ technique [Vassilvitskii and Arthur, 2006], this strategy promotes diversity among initial particles by iteratively choosing the next particle among the MCMC draws with probability proportional to its VI distance from the closest already chosen particle. This increases the likelihood that the  $L$  initial particles will be well separated in partition space, which often leads to better local optima. The computational cost of this step is  $O(TnL)$ , corresponding to computing the VI distance between every MCMC draw and particle. Again thinning is applied by default to reduce the cost in  $T$ . Note that ++ initialization does not require passing in or storing the posterior similarity matrix. In practice, this initialization requires multiple runs; however if the number of runs is sufficiently large, it often provides the best solution (smallest Wasserstein distance).
- *Lowest EVI Initialization (topvi)*: In this method, the expected VI is computed for all the partitions generated by the average linkage, complete linkage, and (if supplied) fixed initialization methods. The  $L$  best partitions among these (with lower EVI) are then selected as initial centers. This approach combines average and complete linkage for a wider set of initial particles. The computational cost is similar to average or complete linkage initialization (multiplied by a factor of two).
- *Fixed Initialization*: This strategy allows the user to directly specify a set of  $L$  fixed partitions to be used as initial centers. This is useful, for example, if the user wishes to include certain known clusterings (such as the minVI, MAP, Binder, or ARI estimators or expert-proposed solutions) as initial candidates.

A detailed description is provided in Algorithm 2. Note that the *N-update* step includes an optional *outlier-search* step, applicable if a region of attraction contains only one partition, indicating that the current center is not the closest to any other partition; this step tries to swap the center with a sampled “outlier” partition, i.e. a partition far (in VI sense) from all centers, and checks if the objective improves.

## C Additional material on describing and visualizing the particles

In Section 3.2, we introduce Example 2, where the data is generated from four Gaussian mixtures. We fit a diagonal location-scale Dirichlet Process Mixture model, using the R package `BNPmix` [Corradin et al., 2021], run for 10,000 iterations after a burn-in of 10,000 iterations. In the posterior similarity matrix shown in Figure 8, uncertainty about the number of clusters is apparent, but a subtle pattern of four equal-sized blocks can be observed, even though some of these seem to be often merged together.

---

**Algorithm 2** WASABI: Finding the approximate WASABI posterior (detailed steps)
 

---

**Input:** MCMC samples  $\{\rho^{(t)}\}_{t=1}^T$ , number of particles  $L$ , initialization method `init`, tolerance  $\epsilon$ , maximum number of iterations `max_iter`

**Initialize**  $\rho_{1:L}^*$  using method `init`

$i \leftarrow 0$

**repeat**

$i \leftarrow i + 1$

***N*-update step:**

Compute  $\text{VI}(\rho^{(t)}, \rho_\ell^*)$  for all  $t$  and  $\ell$

Assign each  $\rho^{(t)}$  to the closest center  $\rho_\ell^*$ , and update the region of attraction  $\mathcal{N}_\ell$

**if** any region of attraction  $|\mathcal{N}_\ell| = 0$  **then**

▷ Empty region of attraction

For such  $\ell$ , compute  $p_{\ell,t} \propto \text{VI}(\rho^{(t)}, \rho_\ell^*)$

Sample  $t^*$  from  $1, \dots, T$  according to  $p_{\ell,t}$

Set  $\rho_\ell^* \leftarrow \rho^{(t^*)}$  and  $\mathcal{N}_\ell \leftarrow \{t^*\}$

***Outlier-check* step:**

**if** any region of attraction  $|\mathcal{N}_\ell| = 1$  **then**

For such  $\ell$ , compute  $p_{\ell,t} \propto \min_{\ell'} \text{VI}(\rho^{(t)}, \rho_{\ell'}^*)$

Sample  $t^*$  from  $1, \dots, T$  according to  $p_{\ell,t}$

**if** objective decreases upon replacement **then**

Set  $\rho_\ell^* \leftarrow \rho^{(t^*)}$  and  $\mathcal{N}_\ell \leftarrow \{t^*\}$

***VI-search* step:**

**for**  $\ell$  in  $1, \dots, L$  **do**

Update centers:  $\rho_\ell^* \leftarrow \text{MINVI}(\mathcal{N}_\ell)$

▷ Different search-algorithms can be used

Update centers' expected-VI:  $l_\ell \leftarrow \text{EVI}(\rho_\ell^*, \mathcal{N}_\ell)$

Update weights  $w_\ell \leftarrow |\mathcal{N}_\ell|/T$

Update loss  $W \leftarrow \sum_{\ell=1}^L w_\ell \cdot l_\ell$

**until** change of  $W$  is less than  $\epsilon$  or  $i > \text{max\_iter}$ .

**Return**  $\{\rho_1^*, \dots, \rho_L^*\}, \mathbf{w} = (w_1, \dots, w_L)$

---

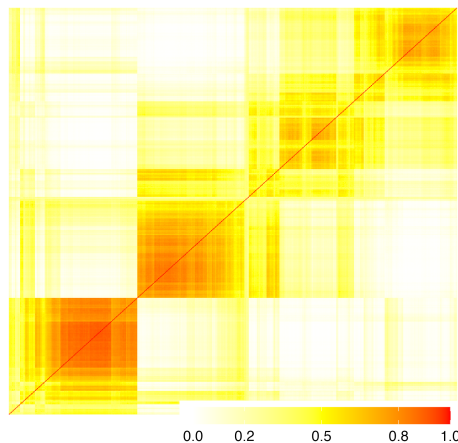


Figure 8: Posterior similarity matrix for the two-dimensional Gaussian mixture with four components (Example 2).

**Visualization of the particles' posterior similarity matrices** Figure 9 displays the posterior similarity matrices (PSMs) for the regions of attraction associated with each WASABI particle in Example 2. While Figure 3b (in Section 3.2) presents PSMs labeled by each particle's own clusters (providing insight into the uncertainty structure around each specific clustering), here, the rows and

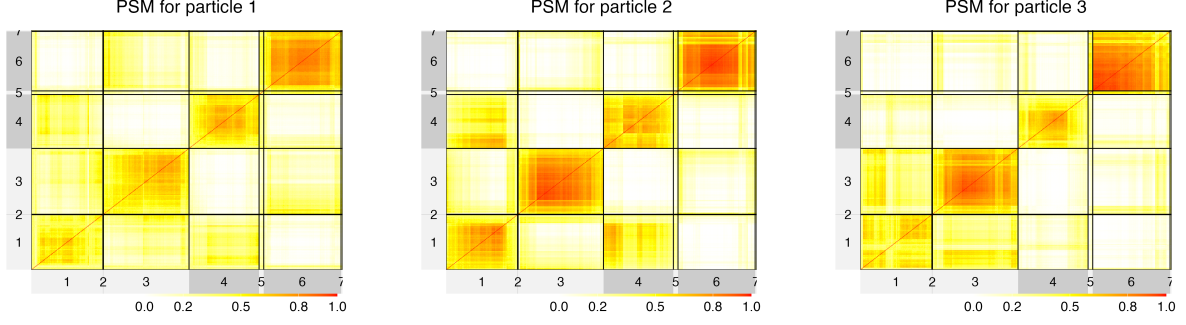


Figure 9: Posterior similarity matrices for each region of attraction corresponding to the WASABI particles in Example 2. In each heatmap, rows and columns are labeled according to the meet’s clusters, enabling direct comparison of the PSM structure across different regions of attraction.

columns are labeled according to the clusters defined by the meet of all particles. This common labeling facilitates direct comparison of cluster uncertainty across different regions of attraction, helping to identify points or groups whose allocation is most variable or most consistent between the particles represented by the WASABI summary.

### C.1 Contribution to the VI

To gain an understanding of the uncertainty in the allocation of each data point in a particular clustering, we compute each data point’s *contribution* to the expected VI. This can be computed by first recalling that the VI Meilă [2007] between two clusterings  $\rho_1$  and  $\rho_2$  is defined as:

$$\begin{aligned} \text{VI}(\rho_1, \rho_2) &= \text{H}(\rho_1) + \text{H}(\rho_2) - 2\text{MI}(\rho_1, \rho_2) \\ &= - \sum_{j_1=1}^{K_1} \frac{n_{j_1,+}}{n} \log_2 \left( \frac{n_{j_1,+}}{n} \right) - \sum_{j_2=1}^{K_2} \frac{n_{+,j_2}}{n} \log_2 \left( \frac{n_{+,j_2}}{n} \right) - 2 \sum_{j_1=1}^{K_1} \sum_{j_2=1}^{K_2} \frac{n_{j_1,j_2}}{n} \log_2 \left( \frac{n_{j_1,j_2} n}{n_{j_1,+} n_{+,j_2}} \right), \end{aligned}$$

where the first two terms represent the entropy of the two clusterings and the last term is the mutual information between the clusterings. The counts  $n_{j_1,j_2}$  represent the cross-tabulation between the clusterings, i.e.  $n_{j_1,j_2}$  is the number of data points in cluster  $j_1$  in  $\rho_1$  and cluster  $j_2$  in  $\rho_2$ , and  $K_1$  and  $K_2$  are the number of clusters in  $\rho_1$  and  $\rho_2$ , respectively. We can equivalently express the VI as:

$$\begin{aligned} \text{VI}(\rho_1, \rho_2) &= \sum_{i=1}^n \frac{1}{n} \log_2 \left( \sum_{i'=1}^n \frac{\mathbf{1}(c_{1,i} = c_{1,i'})}{n} \right) + \sum_{i=1}^n \frac{1}{n} \log_2 \left( \sum_{i'=1}^n \frac{\mathbf{1}(c_{2,i} = c_{2,i'})}{n} \right) \\ &\quad - 2 \sum_{i=1}^n \frac{1}{n} \log_2 \left( \sum_{i'=1}^n \frac{\mathbf{1}(c_{1,i} = c_{1,i'}, c_{2,i} = c_{2,i'})}{n} \right), \end{aligned}$$

where  $c_{1,i}$  and  $c_{2,i}$  represent the allocation of the  $i$ th data point, for  $i = 1, \dots, n$ , in the clusterings  $\rho_1$  and  $\rho_2$  respectively. Therefore, we define the contribution of the  $i$ th data point to the VI between  $\rho_1$  and  $\rho_2$  in Definition 6.

**Definition 6** (Contribution to the VI). *The contribution of the  $i$ th data point to the VI between the clusterings  $\rho_1$  and  $\rho_2$  is*

$$\begin{aligned} \text{VIC}_i(\rho_1, \rho_2) &= \frac{1}{n} \left[ \log_2 \left( \sum_{i'=1}^n \frac{\mathbf{1}(c_{1,i} = c_{1,i'})}{n} \right) + \log_2 \left( \sum_{i'=1}^n \frac{\mathbf{1}(c_{2,i} = c_{2,i'})}{n} \right) \right. \\ &\quad \left. - 2 \log_2 \left( \sum_{i'=1}^n \frac{\mathbf{1}(c_{1,i} = c_{1,i'}, c_{2,i} = c_{2,i'})}{n} \right) \right], \end{aligned}$$

and the VI distance is:

$$VI(\rho_1, \rho_2) = \sum_{i=1}^n VIC_i(\rho_1, \rho_2).$$

When comparing two clusterings (e.g. two particles), this can be useful to understand which data points contribute most to the distance, as well as those with zero (or low) contribution, whose allocation is the same between the two clusterings. Note that a desirable property of the VI is that it is *aligned* with the lattice of partitions. Specifically, it is both *vertically aligned* in the Hasse diagram: if  $\rho_1 \geq \rho_2 \geq \rho_3$ , then the distance between  $\rho_1$  and  $\rho_3$  is the vertical sum of the distances between  $\rho_1$  and  $\rho_2$  and between  $\rho_2$  and  $\rho_3$ , as well as *horizontally aligned*: the distance between any two partitions  $\rho_1$  and  $\rho_2$  is the horizontal sum of the distances between each partition and the meet of the two partitions. Thus, we have that the VI contribution will be the same for all data points belonging to same cluster in the meet  $\rho_1 \wedge \rho_2$ ; allowing for more efficient computation.

Further, we define the contribution of the  $i$ th data point to the expected VI of a clustering  $\rho^*$  in Definition 7.

**Definition 7** (Contribution to the EVI). *The contribution of the  $i$ th data point to the EVI of the clustering  $\rho^*$  is*

$$EVIC_i(\rho^*) = \frac{1}{n} \left[ \log_2 \left( \sum_{i'=1}^n \frac{\mathbf{1}(c_i^* = c_{i'}^*)}{n} \right) + \mathbb{E} \left[ \log_2 \left( \sum_{i'=1}^n \frac{\mathbf{1}(c_i = c_{i'})}{n} \right) \mid \mathbf{y} \right] \right. \\ \left. - 2 \mathbb{E} \left[ \log_2 \left( \sum_{i'=1}^n \frac{\mathbf{1}(c_i^* = c_{i'}^*, c_i = c_{i'})}{n} \right) \mid \mathbf{y} \right] \right],$$

where the expectation is taken with respect to  $\pi(\rho \mid \mathbf{y})$ , the posterior distribution over the space of clusterings. The EVI of  $\rho^*$  is:

$$EVI(\rho^*) = \sum_{i=1}^n EVIC_i(\rho^*).$$

**Remark** (Approximating the contribution to the EVI). *Computing the contribution of the  $i$ th data point the EVI of  $\rho^*$  requires computing the expectation with respect to the posterior over the space of partitions. This can be approximated either based on the MCMC draws:*

$$\widehat{EVIC}_i(\rho^*) = \frac{1}{n} \left[ \log_2 \left( \sum_{i'=1}^n \frac{\mathbf{1}(c_i^* = c_{i'}^*)}{n} \right) + \frac{1}{T} \sum_{t=1}^T \log_2 \left( \sum_{i'=1}^n \frac{\mathbf{1}(c_i^{(t)} = c_{i'}^{(t)})}{n} \right) \right. \\ \left. - 2 \frac{1}{T} \sum_{t=1}^T \log_2 \left( \sum_{i'=1}^n \frac{\mathbf{1}(c_i^* = c_{i'}^*, c_i^{(t)} = c_{i'}^{(t)})}{n} \right) \right],$$

or based on the WASABI posterior:

$$\widehat{\widehat{EVIC}}_i(\rho^*) = \frac{1}{n} \left[ \log_2 \left( \sum_{i'=1}^n \frac{\mathbf{1}(c_i^* = c_{i'}^*)}{n} \right) + \sum_{l=1}^L w_l \log_2 \left( \sum_{i'=1}^n \frac{\mathbf{1}(c_{l,i}^* = c_{l,i'}^*)}{n} \right) \right. \\ \left. - 2 \sum_{l=1}^L w_l \log_2 \left( \sum_{i'=1}^n \frac{\mathbf{1}(c_i^* = c_{i'}^*, c_{l,i}^* = c_{l,i'}^*)}{n} \right) \right].$$

Approximating the contribution of the  $i$ th data point to the EVI based on the WASABI posterior has a clear computational advantage ( $O(nL)$  as opposed to  $O(nT)$  with  $L \ll T$ ); in addition, note that when  $\rho^*$  is one of the particles, every data point in the same cluster of the meet will have the same contribution to the VI, further reducing computations and enhancing interpretation. For example, clusters in the meet with a Wasserstein-VI approximated EVI of zero, are always clustered together and never with any other data points, across all particles.

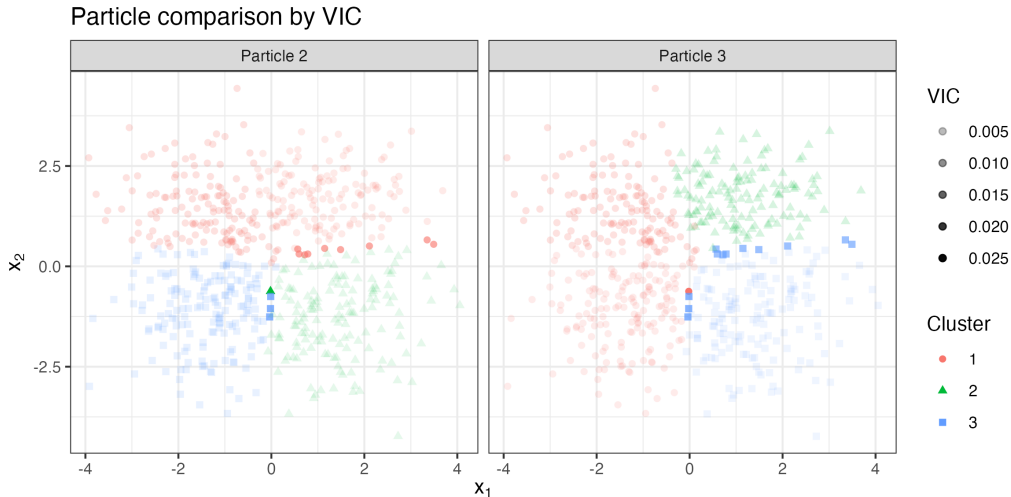


Figure 10: Side-by-side visualization of particles 2 and 3 from Example 2, with points colored by cluster assignment and shaded by their VI contribution (VIC). More solid points indicate higher VIC, highlighting areas where cluster assignments differ most between the particles; greater transparency corresponds to lower VIC and greater agreement.

Figure 10 provides a visual illustration of the pointwise VI contributions (VIC) when comparing particles 2 and 3 from Example 2. In this side-by-side plot, each data point is colored by its cluster assignment in the two particles, with shading indicating the magnitude of its contribution to the overall VI distance: solid points represent higher VIC values, while more transparent points indicate lower contributions. This visualization helps to pinpoint the specific data points (often located at the boundaries of clusters or those reassigned between clusters) that are most responsible for the differences between the two clustering solutions.

**VI Contribution by Group (VICG)** Recall from Section 3.2 that the VI contribution by group (VICG) aggregates the pointwise VI contributions for all data points within each cluster of the meet between two partitions. This provides a higher-level summary of how much each cluster in the meet contributes to the overall VI between two partitions. While individual pointwise VIC values can highlight subtle individual differences in clustering, the VICG effectively reveals more global structural changes, such as when a large cluster is split or merged differently across partitions.

Figure 11 visualizes the VICG for the comparison between particles 2 and 3 in Example 2. Unlike the pointwise VI contribution, which tends to emphasize small, local differences, the VICG highlights broader, high-level discrepancies between partitions. In this example, the meet clusters with the highest VICG, such as the top left component, correspond to large groups that undergo major changes—here, being merged with different components across the two particles. This groupwise perspective makes it easier to identify substantial structural differences in clustering solutions.

## D Experiments: additional material

### D.1 Slightly bimodal example

We consider the slightly bimodal example of Rajkowski [2019] with  $n = 600$  data points generated independently from a mixture of two Gaussians:

$$Y_i \stackrel{\text{iid}}{\sim} 0.5N(-1.1, 1) + 0.5N(1.1, 1).$$

Rajkowski [2019] focuses on the behavior of the MAP clustering when using a DP mixture of Gaussians and, in this example, shows that the partition with a single cluster has higher posterior mass than the intuitive partition of the data into two groups based on positive and negative observed values.

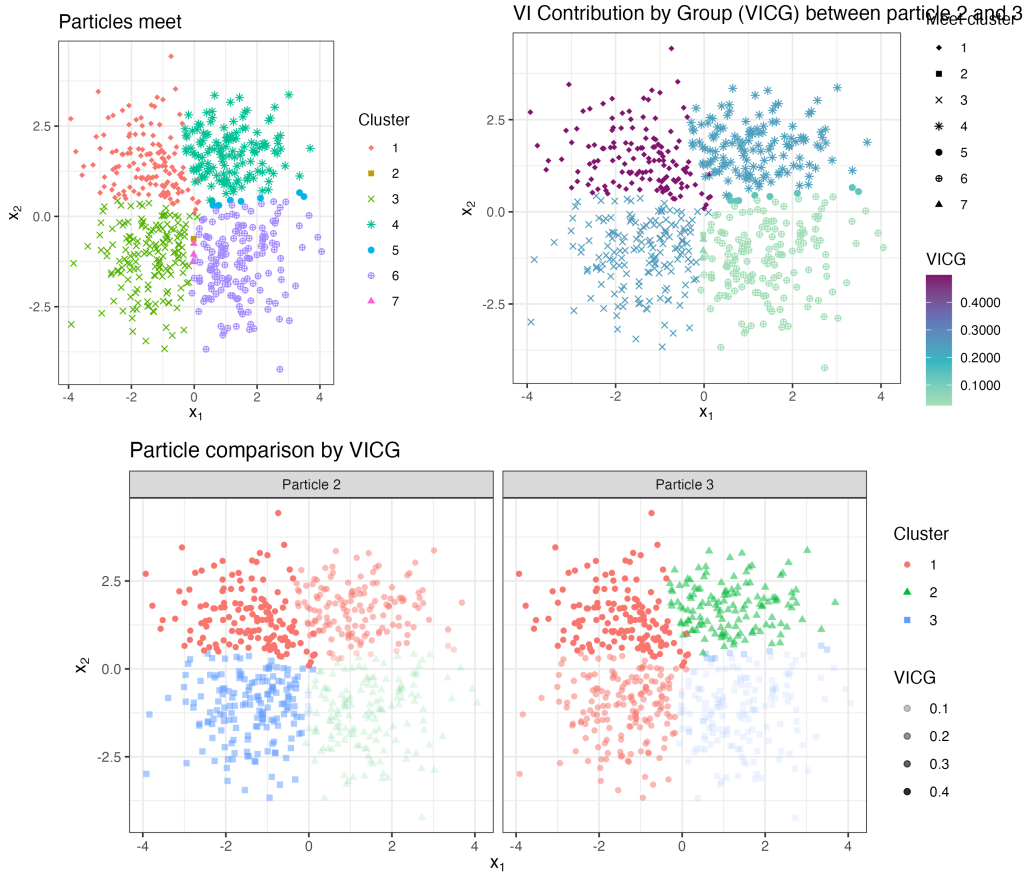


Figure 11: Visualization of VI contribution by group (VICG) between particles 2 and 3 in Example 2. The top left panel displays the cluster assignments defined by the meet of the two partitions, which in this case coincides with the meet of the three particles. The top right panel shows the VICG values for each meet cluster, quantifying the aggregate contribution of each group to the overall VI distance between the two partitions. The bottom panel provides a side-by-side comparison of the two particles, colored by cluster assignment and with transparency reflecting the VIC for each data point. Together, these panels highlight which subsets of data account for the largest discrepancies between the two clustering solutions.

A Dirichlet process mixture of Gaussians is fit to data via the `BNPmix` package [Corradin et al., 2021]. Specifically, the model assumes

$$\begin{aligned}
 Y_i | P &\stackrel{\text{iid}}{\sim} \sum_{j=1}^{\infty} w_j N(\mu_j, \sigma_j^2), \\
 \mu_j | \sigma_j^2 &\stackrel{\text{ind}}{\sim} N\left(\mu_0, \frac{1}{k_0} \sigma_j^2\right), \\
 \sigma_j^2 &\stackrel{\text{iid}}{\sim} \text{IG}(a_0, b_0), \\
 w_j &= v_j \prod_{h < j} (1 - v_h), \text{ with } v_j \stackrel{\text{iid}}{\sim} \text{Beta}(1, \alpha),
 \end{aligned}$$

with  $\mu_0$  set to the sample mean,  $k_0$  set to 0.1 to increase prior variability of the cluster centers,  $a_0 = 3/2$  resulting in a marginal Student t prior on  $\mu_j$  with 3 degrees of freedom, and  $b_0$  equal to the sample variance divided by 4. We consider two different choices of the DP parameter  $\alpha$ : 1)  $\alpha = 1$  which is a commonly-used setting, and 2)  $\alpha = 2/\log(n)$ . The latter choice is motivated by Ascolani et al. [2023], who show that under regularity conditions, the marginal posterior of the number of clusters in the DPM can recover the truth, if  $\alpha$  is tuned via an empirical or hierarchical approach.

This example illustrates a paradox in BNP, where both overestimation and underestimation of the

DP parameter	Median [95% CI]	MAP	VI	VI.lb	Binder	ARI
$\alpha = 1$	7 [3,11]	1	1	2	59	4
$\alpha = 2/\log(n)$	4 [2,6]	1	1	2	2	2

Table 1: Slightly bimodal example. A comparison of the marginal posterior on the number of clusters (posterior median and 95% HPD credible interval) with the number of clusters in the MAP, VI, lowerbound to the VI (VI.lb), Binder, and ARI clustering estimates, for two choices of  $\alpha = 1$  and the empirical choice of  $\alpha = 2/\log(n)$ .

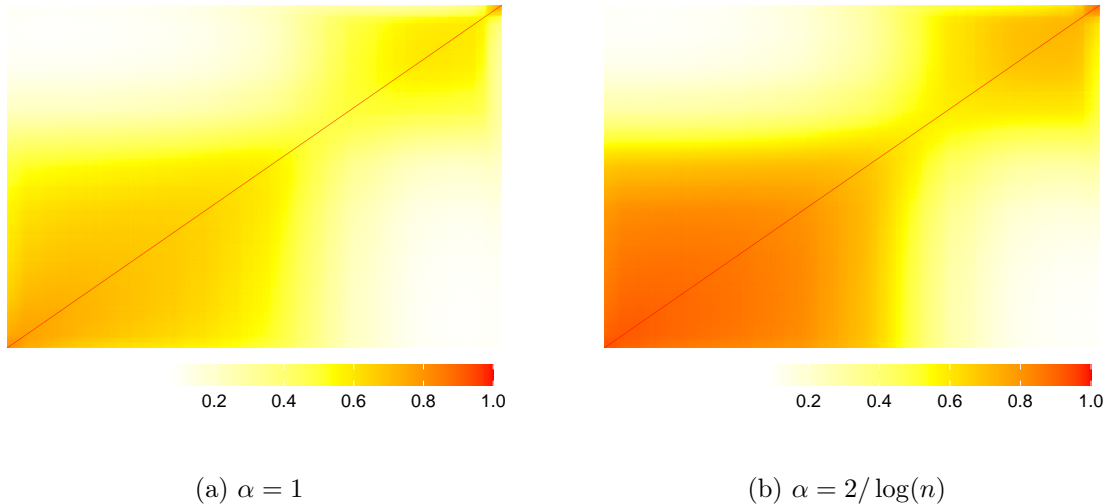


Figure 12: Posterior similarity matrix for the slightly bimodal example for two choices of the DP parameter.

number of clusters occurs depending on how one choose to summarize the posterior. Specifically, it has been shown that the marginal posterior on the number of clusters can suffer from overestimation and inconsistency for the number of clusters if  $\alpha$  is not properly tuned [Miller and Harrison, 2013, 2014, Ohn and Lin, 2023, Ascolani et al., 2023, Alamichel et al., 2024]. In agreement with this, the 95% highest posterior density credible interval for the number of clusters shows overestimation when  $\alpha = 1$  in this slightly bimodal example, but contains the true number of clusters for the empirical choice of  $\alpha$  (Table 1). Despite this, the optimal clustering estimate can still recover the truth under appropriate choice of loss [Rajkowski, 2019, Wade, 2023]. However, in this example when the clusters are not well separated, the MAP and VI estimate contain only a single cluster, regardless of  $\alpha$ , while Binder and ARI overestimate the number of clusters for  $\alpha = 1$  and recover the true number for the empirical choice of  $\alpha$  (Table 1). Interestingly, in previous literature, agreement was observed between the clustering solutions which minimize the expected VI and its more computationally efficient lower bound [Wade and Ghahramani, 2018]; however, in this slightly bimodal example, they disagree, with the latter reporting two clusters (for both choices of  $\alpha$ ). The posterior similarity matrix (Figure 12) shows greater uncertainty in clustering structure for  $\alpha = 1$ .

The WASABI posterior shows robustness to the choice of  $\alpha$ . For both choices, WASABI’s particles are almost identical, see Figure 13. However, the weights in the WASABI posterior are different, with higher mass on the one-cluster solution for the empirical choice of  $\alpha$  (when the prior is more concentrated on a small number of clusters). Instead, the weights are more equal for  $\alpha = 1$ .

## D.2 Examples in Section 4

In Section 4, we presented experiments with synthetic data under two scenarios where the posterior distribution displays high uncertainty: (1) when the model is correctly specified but the mixture components are not well-separated, and (2) when the model is misspecified. Here, we provide additional details on the data-generating processes for both scenarios.

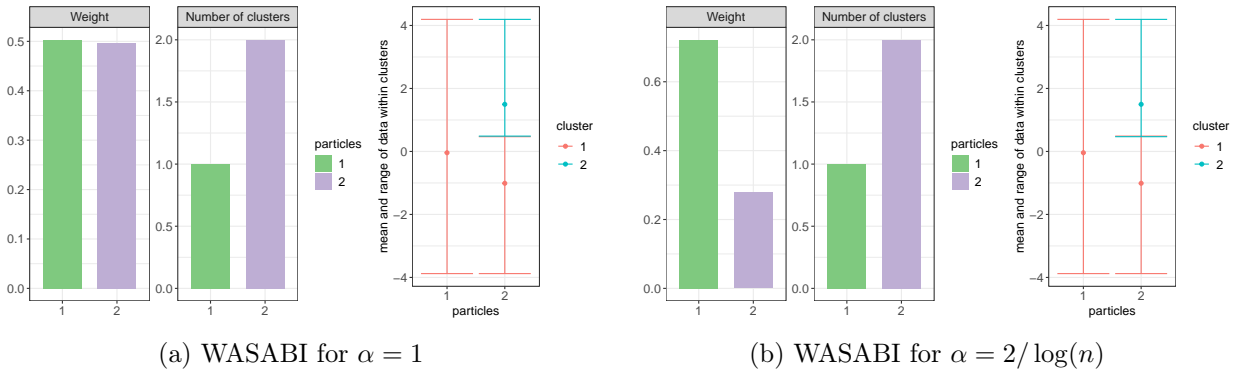


Figure 13: Slightly bimodal example. WASABI’s particles are almost identical for both choices of  $\alpha$  (the second particles differ in the allocation of only two points), but the weights are different, with higher mass on the one-cluster solution for the empirical choice of  $\alpha$  and more equal weights for  $\alpha = 1$  in the WASABI posterior.

For scenario (1), we investigated the impact of cluster separation on posterior uncertainty using datasets where the model is correctly specified but the mixture components have varying degrees of overlap. Each dataset consists of  $n = 600$  observations in two dimensions, drawn from a mixture of four equally weighted Gaussian components. The component means are symmetrically positioned at  $(m, m)$ ,  $(m, -m)$ ,  $(-m, -m)$ , and  $(-m, m)$ , where the separation parameter  $m$  (with identity covariance matrix) controls the distance between clusters. The value of  $m$  was varied across a dense grid to explore a wide range of overlap, specifically  $m \in \{0.1, 0.3, 0.5, 0.7, 0.9, 1.1, 1.3, 1.5, 1.7, 1.9, 2.0, 2.2, 2.4, 2.6, 2.8, 3.0\}$ . For each value of  $m$ , ten independent datasets were generated with different random seeds, with points assigned to each component with equal probability. A graphical representation is provided in Figure 14.

For scenario (2), we evaluated the robustness of WASABI under model misspecification, designing two types of synthetic experiments: (a) data drawn from a Gaussian distribution truncated to the unit square, and (b) data drawn from a two-dimensional skewed- $t$  distribution. In both cases, the aim is to investigate scenarios where a Gaussian mixture model is misspecified for the underlying data and to observe its effect on the posterior distribution and clustering summaries.

For each setting, datasets are generated as follows: for a given parameter configuration,  $n = 200$  data points in  $p = 2$  dimensions are simulated, and the process is repeated for five independent replicates. Each dataset is then analyzed using a (diagonal location-scale) Dirichlet process mixture of Gaussians fit via the `BNPmix` package [Corradin et al., 2021]. Across both types, we explore a grid of parameter values to modulate the severity of misspecification.

Specifically, for setting (a) we consider Gaussian distributions truncated to the unit square  $[0, 1]^2$ . For each standard deviation  $\sigma$  in the set  $\{0.1, 0.2, 0.4, 0.6, 0.8, 1, 3\}$ , data are generated from a normal distribution centered at  $(0.5, 0.5)$  with covariance matrix  $\sigma^2 I$ . Points falling outside the unit square are discarded and resampled until exactly  $n$  points are retained. For small  $\sigma$ , the data is concentrated near the center; as  $\sigma$  increases, the resulting distribution approaches a uniform distribution over the unit square.

For setting (b), each data point is drawn from a two-dimensional skewed- $t$  distribution, using the `rskt` function from the `skewt` package. Parameters are varied over a grid of degrees of freedom  $df \in \{30, 10, 7.5, 5, 3\}$  and skewness parameters  $\gamma \in \{1, 1.5, 2, 3, 5, 10\}$ , covering cases from nearly Gaussian to highly skewed and heavy-tailed. As before, datasets consist of  $n$  points in two dimensions, and the Dirichlet process mixture model is fit using the same approach as in setting (a).

For each dataset generated under any setting, posterior draws are used to compute the posterior similarity matrix and clustering summaries, including minVI and the WASABI approximation.

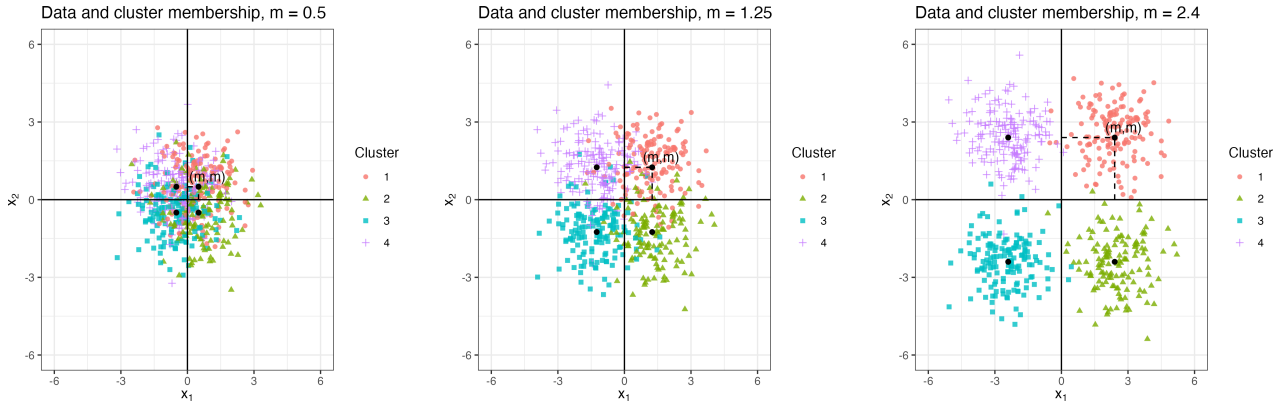


Figure 14: Illustration for the data generating process for scenario (1) in the synthetic experiments. The data is generated from a four-components mixture Gaussian distribution, with each component centered around the points  $(x_i, y_i)$  for  $i = 1, \dots, 4$ , with  $|x_i| = |y_i| = m$ . The covariance matrix for each component is diagonal with marginal variances equal to 1. Three datasets are displayed for different values of the center location parameter  $m$ .

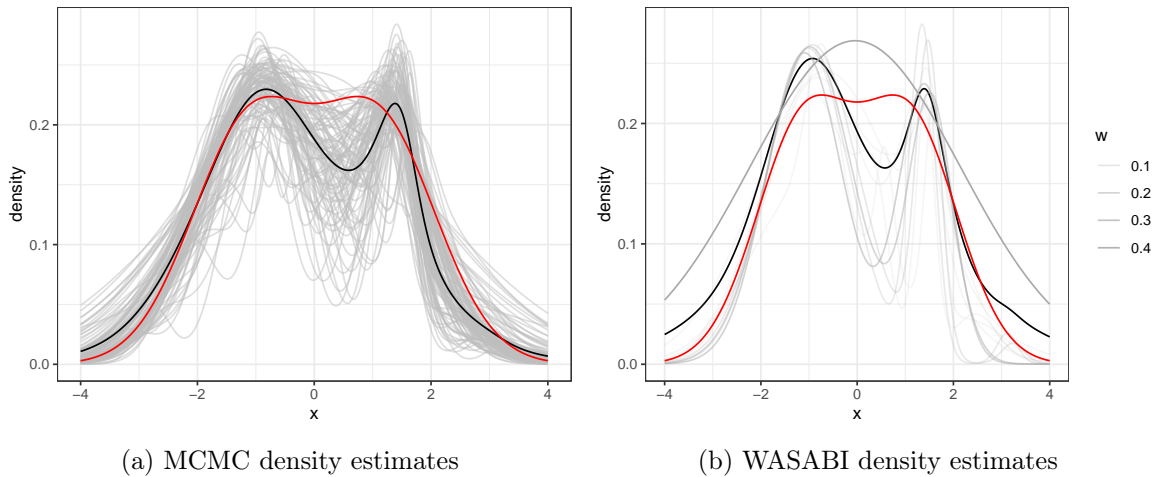


Figure 15: Density estimation (black) for Example 1 based on the MCMC samples and WASABI posterior, with the true data-generating density in red. For MCMC, the densities for a subset of MCMC draws are shown in gray, and for WASABI, the density for each particle is shown in gray with opacity determined by the particle's weight.

### D.3 Posterior compression

WASABI is useful for improved understanding of the posterior but could also be relevant for posterior compression in order to reduce both storage and the computational cost of predictive inference. For storage, saving only the WASABI particles and weights as opposed to all MCMC samples, reduces storage costs from  $O(nT)$  to  $O(nL)$ , with  $L \ll T$ . Predictive inference involves computing the predictive quantity of interest for every MCMC sample and all new points; for example, density estimation for multivariate Gaussian mixtures is  $O(Tn^*p^2K_{\max})$ , where  $n^*$  is the number of new points where the density is to be evaluated (often a large grid) and  $K_{\max}$  is the maximum number of clusters. If we are interested in conditional density estimation as in the HPV uptake study of Section 5, this becomes even more expensive as we must evaluate the density on grid of  $y$  values for every covariate value considered.

For illustration, consider the task of density estimation for Example 1. While the MCMC-based estimates are slightly better than the WASABI-based ones (Figure 15), WASABI significantly reduces the cost by a factor of 1,000 (Table 2).

Approximation method	$L_1$ distance	Wall-clock time (sec)
MCMC	0.127	1601.9
WASABI	0.191	1.7

Table 2: Density estimation for Example 1 based on an MCMC and WASABI approximation, comparing the tradeoff between low error (measured by the approximate  $L_1$  distance between the true and estimated density) and run time.

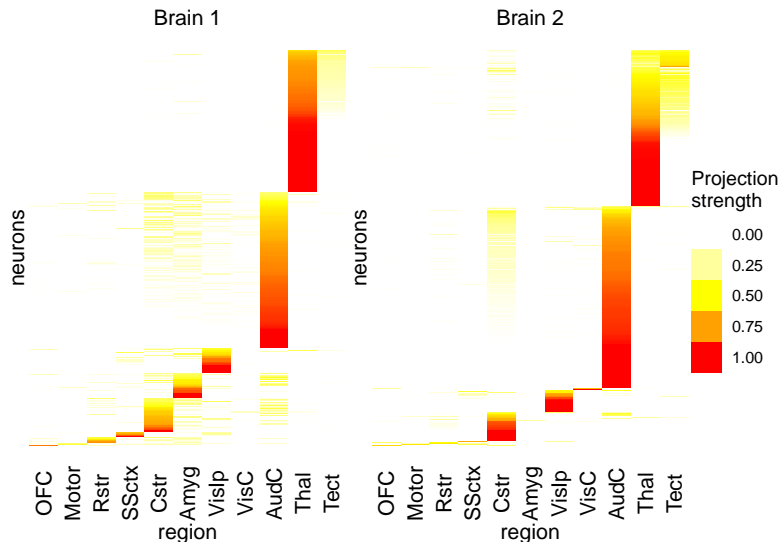


Figure 16: Heatmap of the empirical projection strength (computed as the neuron’s barcode counts divided by its total count), with rows representing neurons and columns corresponding to the 11 target areas.

## E Real data analysis

### E.1 Investigating projection patterns at the single-neuron resolution

The auditory cortex data [Chen et al., 2019] illustrated in Figure 16 suggests diversity in the projections of neurons. HBMAP [Wade et al., 2025] employs a hierarchical Bayesian mixture of Dirichlet-multinomials to directly model the count data, effectively integrate data across brains, and identify projection patterns. In the MCMC algorithm of HBMAP, we combine five parallel runs with the number of iterations to 20,000, burn-in of 10,000 and thinning of 5, resulting in 10,000 posterior samples of partitions. The marginal posterior on the number of clusters is concentrated around 22-32; the optimal clustering estimate contains 27, 37, and 50 clusters under the VI, ARI, and Binder’s loss; and the posterior similarity matrix suggests both stability but also uncertainty in clusters (see Figure 17).

To better understand and summarize uncertainty in the clustering structure and projection patterns, we use WASABI with  $L = 3$  particles (see elbow plot in Figure 18a). The particles all have substantial weights, and the number of clusters in each particle ranges from 27 to 31 (Figure 18b). The clusters and projection patterns associated to each particle are illustrated in Figure 7 of the main text. This highlights how particle 2 mainly differs from particle 1, for example, by 1) expanding the cluster with high projection strength to AudC and low strength to Cstr and Amyg ( $\uparrow$ AudC,  $\downarrow$ Cstr,  $\downarrow$ Amyg) to include additional neurons with low projection strength to other areas in the ipsilateral cortex; and 2) redistributing some neurons in the (Thal, Tect) motif to the ( $\uparrow$ Thal,  $\downarrow$ Tect) motif, suggesting that the separation between these groups may be less defined. In addition, we can appreciate how particle 3 differs from particle 1 by 1) splitting off a small group of neurons from the ( $\uparrow$ AudC,  $\downarrow$ Cstr,  $\downarrow$ Amyg) with weaker strength to AudC; 2) reallocating some of the neurons among the (Thal, Tect), ( $\uparrow$ Thal,  $\downarrow$ Tect), and (Thal, Tect,  $\downarrow$ Cstr) motifs.

The collapsed WASABI posterior similarity matrix (top left in Figure 18) highlights how the 54 clusters in the meet are co-clustered across the three particles, with the y-axis showing how they are

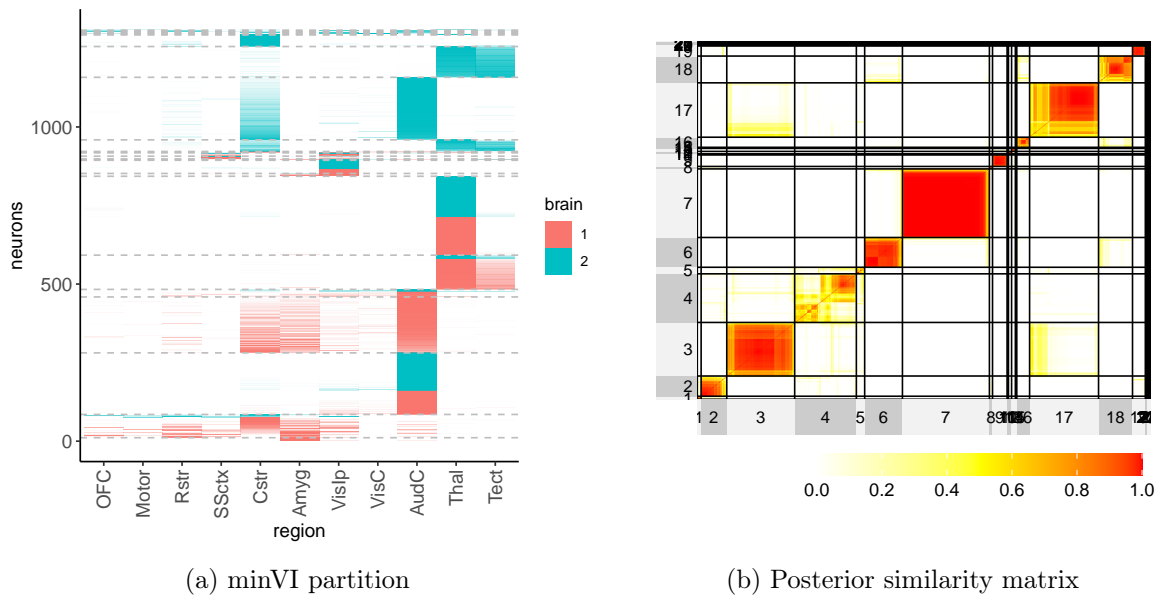


Figure 17: Neurons belonging to different clusters of the minVI partition are separated by dashed lines in the heatmap of the data in Panel 17a and by solid lines in the posterior similarity matrix in Panel 17b.

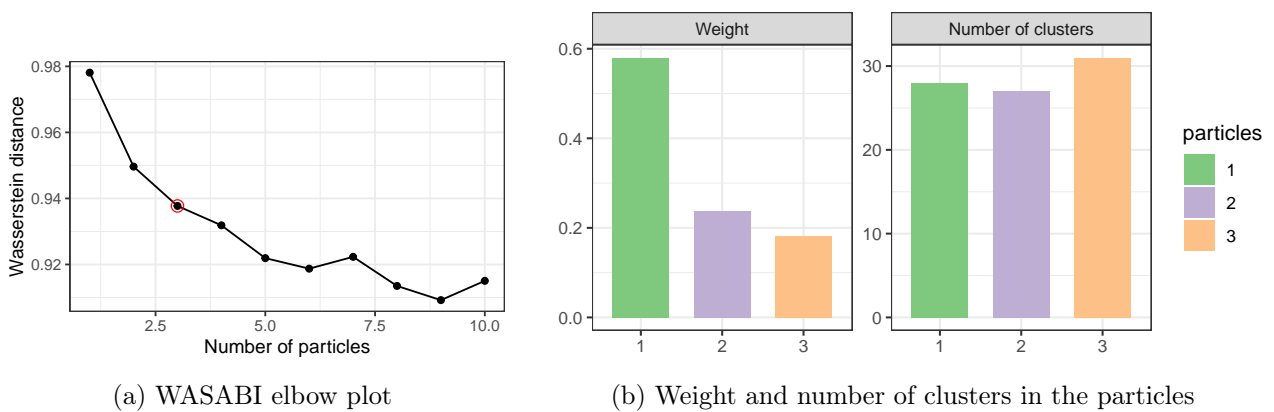


Figure 18: The elbow plot of the Wasserstein distance against the number of particles suggests  $L = 3$  particles (Panel 18a). The weight and number of clusters in each of the particles is shown in Panel 18b.

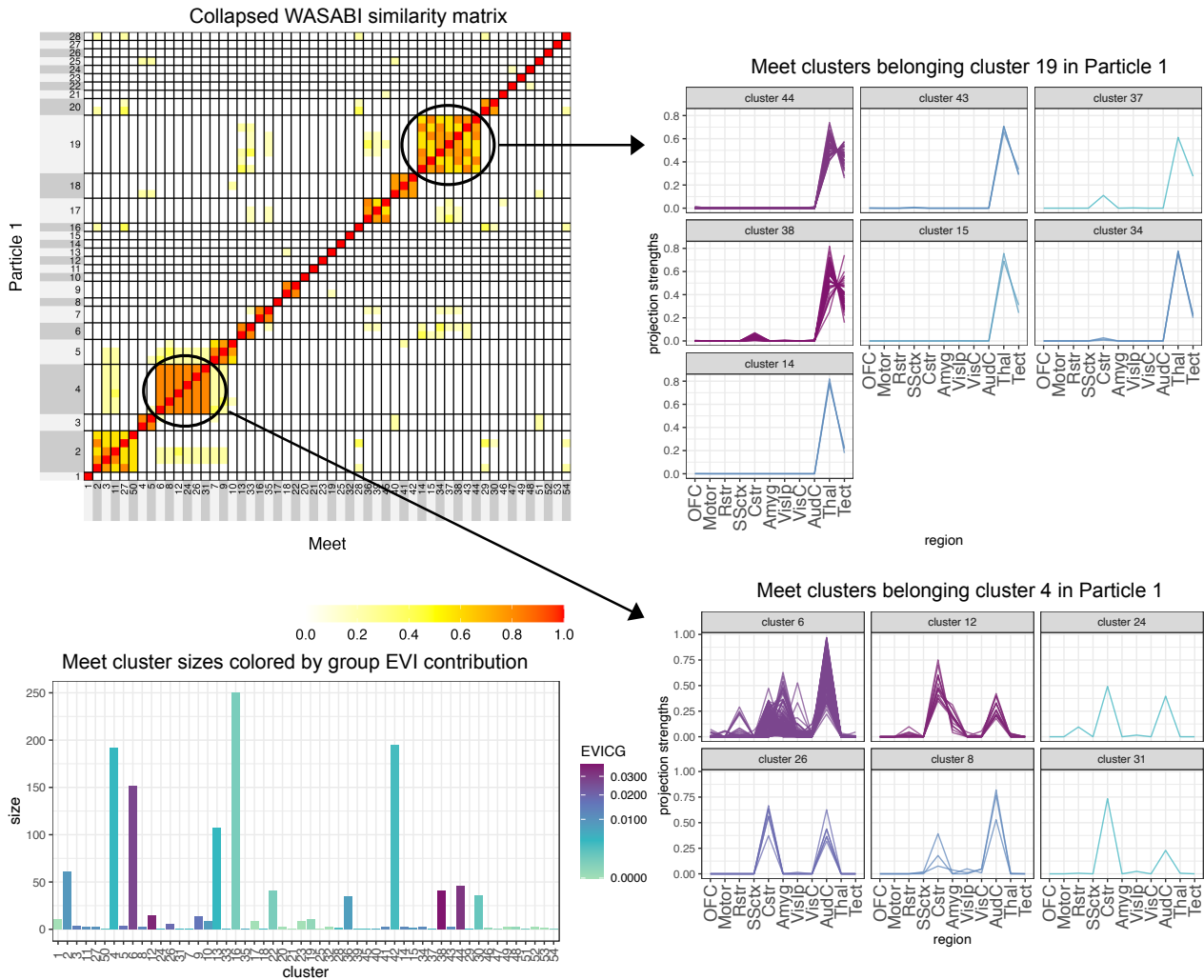
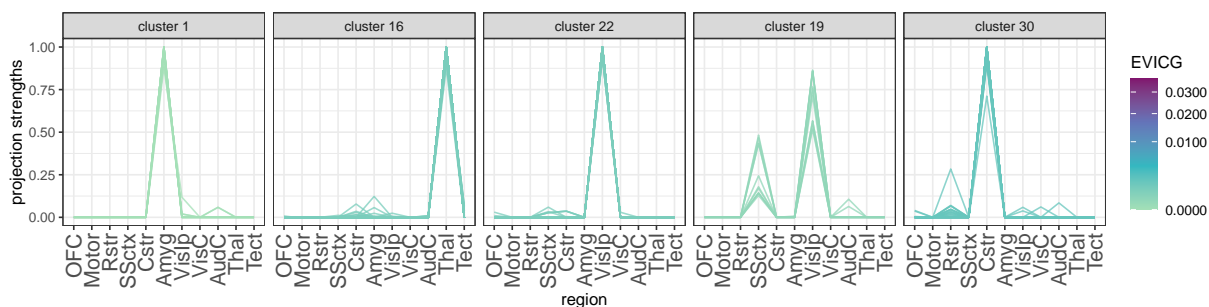
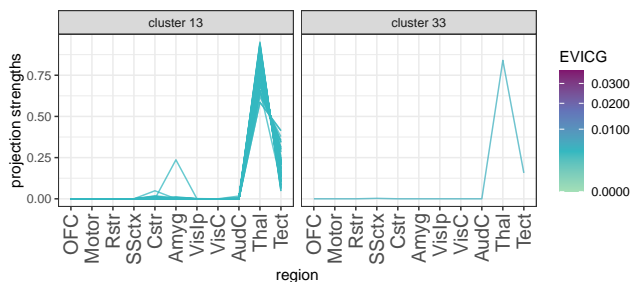


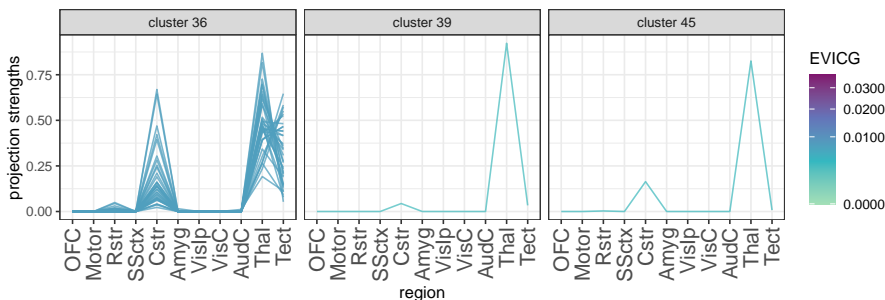
Figure 19: Summarizing uncertainty in projection patterns from the auditory cortex. Top left: collapsed WASABI posterior similarity matrix illustrates how the 54 clusters in the meet are co-clustered across the three particles, with the y-axis showing how they are grouped together in the first particle. Bottom left: bar chart of the sizes of meet clusters, with color representing the total contribution of the neurons in each meet cluster to the EVI of the meet based on the WASABI posterior. Top right: line plots of the empirical projection strength (barcode counts divided by the neuron’s total count) of neurons in meet clusters grouped into cluster 19 of particle 1, colored by the EVIC of the meet cluster; in particle 1, this motif characterizes neurons projecting to Thal and Tect. Bottom right: lines plots of neurons in meet clusters grouped together in cluster 4 of particle 1; in particle 1 this characterizes the ( $\uparrow$ AudC,  $\downarrow$ Cstr,  $\downarrow$ Amyg) motif.



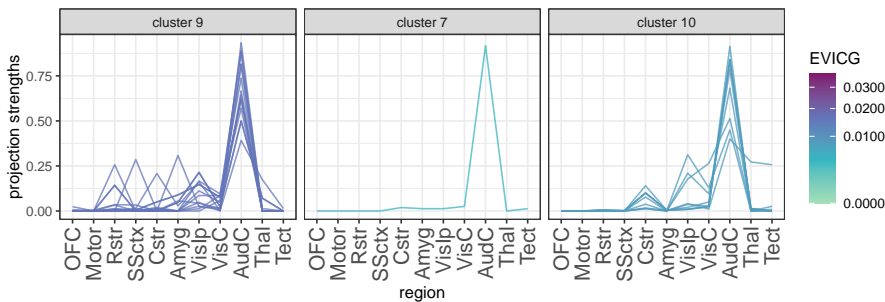
(a) Stable meet clusters with low group contribution to the EVI



(b) Meet clusters grouped into a ( $\uparrow$ Thal,  $\downarrow$ Tect) motif particle 1



(c) Meet clusters grouped into a (Thal, Tect,  $\downarrow$ Cstr) motif in particle 1



(d) Meet clusters grouped into a ( $\uparrow$ AudC,  $\downarrow$ Rstr,  $\downarrow$ Cstr,  $\downarrow$ Amyg,  $\downarrow$ VisIp,  $\downarrow$ VisC,  $\downarrow$ Thal) motif in particle 1

Figure 20: Line plots (normalized barcode counts across target areas) for neurons within certain meet clusters, with neurons colored by the group contribution to the EVI of the meet. Panel 20a: meet clusters that are stable across particles have low group contribution to the EVI of the meet ( $\text{EVICG} < 0.002$ ). Panel 20b: meet clusters that are grouped together in cluster 6 of particle 1 to form a (Thal, Tect,  $\downarrow$ Cstr) motif. Panel 20c: meet clusters that are grouped together in cluster 17 of particle 1 to form a (Thal, Tect,  $\downarrow$ Cstr) motif. Panel 20d: meet clusters that are grouped together in cluster 5 of particle 1 to form a ( $\uparrow$ AudC,  $\downarrow$ Rstr,  $\downarrow$ Cstr,  $\downarrow$ Amyg,  $\downarrow$ VisIp,  $\downarrow$ VisC,  $\downarrow$ Thal) motif.

grouped together in the first particle. Some meet clusters are quite small, corresponding to neurons which may have atypical projection patterns or those with projections that are between groups, while other meet clusters contain a sizable number of neurons (see bottom left in Figure 18). In fact, five sizable clusters stand out as distinct projection patterns, with very low contribution to the EVI of the meet (Figure 20a shows meet clusters with at least 10 neurons and  $EVICG < 0.002$ ); this includes three motifs that target a single region only (Amyg, Thal, Vislp) and two motifs that target two areas, namely, a ( $\uparrow$ Vislp,  $\downarrow$ SSctx) motif and ( $\uparrow$ Cstr,  $\downarrow$ Rstr) motif. Instead, the other sizable meet clusters are often grouped together in slightly different ways across the particles.

For example, focusing on the meet clusters that are grouped into cluster 4 of particle 1 forming a ( $\uparrow$ AudC,  $\downarrow$ Cstr,  $\downarrow$ Amyg) motif, we can appreciate how some neurons with lower projection strength to AudC or no projection to Amyg may be split or join a different cluster (e.g. meet cluster 12 forms a new cluster in particle 3). In addition, these clusters may be combined with most neurons grouped into cluster 5 of particle 1, forming a motif with high strength to AudC and low strength to other regions (meet clusters grouped into cluster 5 of particle 1 are shown in Figure 20d).

Another interesting example concerns meet clusters that are grouped in cluster 19 (top right of Figure 19), cluster 6 (Figure 20b), and cluster 17 (Figure 20c) in particle 1. These clusters represent corticothalamic neurons that are subdivided into the projection motifs to (Thal, Tect), ( $\uparrow$ Thal,  $\downarrow$ Tect), and (Thal, Tect,  $\downarrow$ Cstr). While these motifs are present across all particles, we observed uncertainty in the allocation of some neurons among these motifs (such as the large meet cluster 38 - in the top right of Figure 19 - which moves from the (Thal, Tect) motif in particle 1 to the (Thal, Tect,  $\downarrow$ Cstr) motif in particle 3). This suggests a fuzzy boundary between these three motifs.

## References

- Louise Alamichel, Daria Bystrova, Julyan Arbel, and Guillaume Kon Kam King. Bayesian mixture models (in) consistency for the number of clusters. *Scandinavian Journal of Statistics*, 51(4):1619–1660, 2024.
- Filippo Ascolani, Antonio Lijoi, Giovanni Rebaudo, and Giacomo Zanella. Clustering consistency with Dirichlet process mixtures. *Biometrika*, 110(2):551–558, 2023.
- Cecilia Balocchi, Sameer K Deshpande, Edward I George, and Shane T Jensen. Crime in Philadelphia: Bayesian clustering with particle optimization. *Journal of the American Statistical Association*, 118(542):818–829, 2023.
- D.A. Binder. Bayesian cluster analysis. *Biometrika*, 65:31–38, 1978.
- David M Blei, Andrew Y Ng, and Michael I Jordan. Latent Dirichlet allocation. *Journal of Machine Learning Research*, 3:993–1022, 2003.
- David Buch, Miheer Dewaskar, and David B Dunson. Bayesian level-set clustering. *arXiv:2403.04912*, 2024.
- Guillermo Canas and Lorenzo Rosasco. Learning probability measures with respect to optimal transport metrics. In *Advances in Neural Information Processing Systems*, volume 25, 2012.
- Xiaoyin Chen, Yu-Chi Sun, Huiqing Zhan, Justus M Kecsichull, Stephan Fischer, Katherine Matho, Z Josh Huang, Jesse Gillis, and Anthony M Zador. High-throughput mapping of long-range neuronal projection using in situ sequencing. *Cell*, 179(3):772–786, 2019.
- Stephen Coleman, Paul DW Kirk, and Chris Wallace. Consensus clustering for Bayesian mixture models. *BMC Bioinformatics*, 23(1):290, 2022.
- Riccardo Corradin, Antonio Canale, and Bernardo Nipoti. BNPmix: An R package for Bayesian nonparametric modeling via Pitman-Yor mixtures. *Journal of Statistical Software*, 100(15):1–33, 2021.

- Marco Cuturi and Arnaud Doucet. Fast computation of Wasserstein barycenters. In *International Conference on Machine Learning*, pages 685–693, 2014.
- David B Dahl, Devin J Johnson, and Peter Müller. Search algorithms and loss functions for Bayesian clustering. *Journal of Computational and Graphical Statistics*, 31(4):1189–1201, 2022.
- D.B. Dahl. Model-based clustering for expression data via a Dirichlet process mixture model. In *Bayesian Inference for Gene Expression and Proteomic*, pages 201–218, 2006.
- Dat Do, Linh Do, Scott A McKinley, Jonathan Terhorst, and XuanLong Nguyen. Dendrogram of mixing measures: Learning latent hierarchy and model selection for finite mixture models. *arXiv:2403.01684*, 2024.
- Edwin Fong, Simon Lyddon, and Chris Holmes. Scalable nonparametric sampling from multimodal posteriors with the posterior bootstrap. In *International Conference on Machine Learning*, pages 1952–1962, 2019.
- Beatrice Franzolini and Giovanni Rebaudo. Entropy regularization in probabilistic clustering. *Statistical Methods & Applications*, 33(1):37–60, 2024.
- A. Fritsch and K. Ickstadt. Improved criteria for clustering based on the posterior similarity matrix. *Bayesian Analysis*, 4:367–392, 2009.
- Sylvia Frühwirth-Schnatter, Gertraud Malsiner-Walli, and Bettina Grün. Generalized mixtures of finite mixtures and telescoping sampling. *Bayesian Analysis*, 16(4):1279–1307, 2021.
- Subhashis Ghosal and Aad Van der Vaart. *Fundamentals of Nonparametric Bayesian Inference*. Cambridge University Press, 2017.
- Clara Grazian. A review on bayesian model-based clustering. *arXiv:2303.17182*, 2023.
- Aritra Guha, Nhat Ho, and XuanLong Nguyen. On posterior contraction of parameters and interpretability in Bayesian mixture modeling. *Bernoulli*, 27(4):2159–2188, 2021.
- J.A. Hartigan and M.A Wong. Algorithm AS 136: A k-means clustering algorithm. *Journal of the Royal Statistical Society: Series C*, 28:100–108, 1979.
- Christian Hennig. What are the true clusters? *Pattern Recognition Letters*, 64:53–62, 2015.
- Nhat Ho and XuanLong Nguyen. On strong identifiability and convergence rates of parameter estimation in finite mixtures. *Electronic Journal of Statistics*, 10(1):271 – 307, 2016.
- Justus M Kebschull, Pedro Garcia da Silva, Ashlan P Reid, Ian D Peikon, Dinu F Albeanu, and Anthony M Zador. High-throughput mapping of single-neuron projections by sequencing of barcoded RNA. *Neuron*, 91(5):975–987, 2016.
- J.W. Lau and P.J. Green. Bayesian model-based clustering procedures. *Journal of Computational and Graphical Statistics*, 16:526–558, 2007.
- Aurore Lavigne and Silvia Liverani. Quantifying the uncertainty of partitions for infinite mixture models. *Statistics & Probability Letters*, 204:109930, 2024. ISSN 0167-7152. doi: <https://doi.org/10.1016/j.spl.2023.109930>.
- A.Y. Lo. On a class of Bayesian nonparametric estimates: I. Density estimates. *Annals of Statistics*, 12:351–357, 1984.
- Steven N MacEachern, Merlise Clyde, and Jun S Liu. Sequential importance sampling for nonparametric Bayes models: The next generation. *Canadian Journal of Statistics*, 27(2):251–267, 1999.
- Gertraud Malsiner-Walli, Sylvia Frühwirth-Schnatter, and Bettina Grün. Model-based clustering based on sparse finite Gaussian mixtures. *Statistics and Computing*, 26(1):303–324, 2016.

- M. Meilă. Comparing clusterings – an information based distance. *J. Multivar. Anal.*, 98:873–895, 2007.
- Jeffrey W Miller and Matthew T Harrison. A simple example of Dirichlet process mixture inconsistency for the number of components. *Advances in Neural Information Processing Systems*, 26, 2013.
- Jeffrey W Miller and Matthew T Harrison. Inconsistency of Pitman-Yor process mixtures for the number of components. *Journal of Machine Learning Research*, 15(1):3333–3370, 2014.
- Jeffrey W Miller and Matthew T Harrison. Mixture models with a prior on the number of components. *Journal of the American Statistical Association*, 113(521):340–356, 2018.
- Peter Müller. Bayesian nonparametric mixture models. *Handbook of Mixture Analysis*, pages 97–116, 2019.
- Khai Nguyen and Peter Müller. Summarizing Bayesian nonparametric mixture posterior – sliced optimal transport metrics for Gaussian mixtures, 2024.
- XuanLong Nguyen. Convergence of latent mixing measures in finite and infinite mixture models. *The Annals of Statistics*, 41(1):370 – 400, 2013.
- Yang Ni, Peter Müller, Maurice Diesendruck, Sinead Williamson, Yitan Zhu, and Yuan Ji. Scalable Bayesian nonparametric clustering and classification. *Journal of Computational and Graphical Statistics*, 29(1):53–65, 2020.
- Agostino Nobile and Alastair T Fearnside. Bayesian finite mixtures with an unknown number of components: The allocation sampler. *Statistics and Computing*, 17(2):147–162, 2007.
- Ilsang Ohn and Lizhen Lin. Optimal Bayesian estimation of Gaussian mixtures with growing number of components. *Bernoulli*, 29(2):1195–1218, 2023.
- Jelili Oyelade, Itunuoluwa Isewon, Funke Oladipupo, Olufemi Aromolaran, Efosa Uwoghiren, Faridah Ameh, Moses Achas, and Ezekiel Adebisi. Clustering algorithms: their application to gene expression data. *Bioinformatics and Biology Insights*, 10:237–253, 2016.
- David Pollard. Quantization and the method of k-means. *IEEE Transactions on Information Theory*, 28(2):199–205, 1982.
- F.A. Quintana and P.L. Iglesias. Bayesian clustering and product partition models. *Journal of the Royal Statistical Society: Series B*, 65:557–574, 2003.
- Łukasz Rajkowski. Analysis of the maximal a posteriori partition in the Gaussian Dirichlet process mixture model. *Bayesian Analysis*, 14(2):477–494, 2019.
- Riccardo Rastelli and Nial Friel. Optimal Bayesian estimators for latent variable cluster models. *Statistics and Computing*, 28(6):1169–1186, 2018.
- Sylvia Richardson and Peter J Green. On Bayesian analysis of mixtures with an unknown number of components (with discussion). *Journal of the Royal Statistical Society: Series B*, 59(4):731–792, 1997.
- Tommaso Rigon, Amy H Herring, and David B Dunson. A generalized Bayes framework for probabilistic clustering. *Biometrika*, 110(3):559–578, 2023.
- María Xosé Rodríguez-Álvarez, Vanda Inácio, and Nadja Klein. Density regression via Dirichlet process mixtures of normal structured additive regression models. *Statistics and Computing*, 35(2):47, 2025.
- Judith Rousseau and Kerrie Mengersen. Asymptotic behaviour of the posterior distribution in overfitted mixture models. *Journal of the Royal Statistical Society: Series B*, 73(5):689–710, 2011.

- Raied Salman, Vojislav Kecman, Qi Li, Robert Strack, and Erik Test. Fast k-means algorithm clustering. *arXiv preprint arXiv:1108.1351*, 2011.
- John A Saunders. Cluster analysis for market segmentation. *European Journal of Marketing*, 14(7):422–435, 1980.
- Sergei Vassilvitskii and David Arthur. k-means++: The advantages of careful seeding. In *Proceedings of the ACM-SIAM Symposium on Discrete Algorithms*, pages 1027–1035, 2006.
- N.X. Vinh, J. Epps, and J. Bailey. Information theoretic measures for clusterings comparison: Variants, properties, normalization and correction for chance. *Journal of Machine Learning Research*, 11:2837–2854, 2010.
- Sara Wade. Bayesian cluster analysis. *Philosophical Transactions of the Royal Society A*, 381(2247):20220149, 2023.
- Sara Wade and Zoubin Ghahramani. Bayesian cluster analysis: Point estimation and credible balls (with discussion). *Bayesian Analysis*, 13(2):559–626, 2018.
- Sara Wade and Vanda Inácio. Bayesian dependent mixture models: A predictive comparison and survey. *Statistical Science*, 40(1):81–108, 2025.
- Sara Wade, Edward Agboraw, Jinlu Liu, Huizi Zhang, and Gülşen Sürmeli. HBMAP: Bayesian inference of neural circuits from DNA barcoded projection mapping. *bioRxiv:666115*, 2025. doi: 10.1101/2025.07.24.666115.
- Yuling Yao, Aki Vehtari, and Andrew Gelman. Stacking for non-mixing Bayesian computations: The curse and blessing of multimodal posteriors. *Journal of Machine Learning Research*, 23(79):1–45, 2022.
- Michael Minyi Zhang and Sinead A Williamson. Embarrassingly parallel inference for Gaussian processes. *Journal of Machine Learning Research*, 20(169):1–26, 2019.